iScience

CellPress
OPEN ACCESS

Article

Secretory defects in pediatric osteosarcoma result from downregulation of selective COPII coatomer proteins

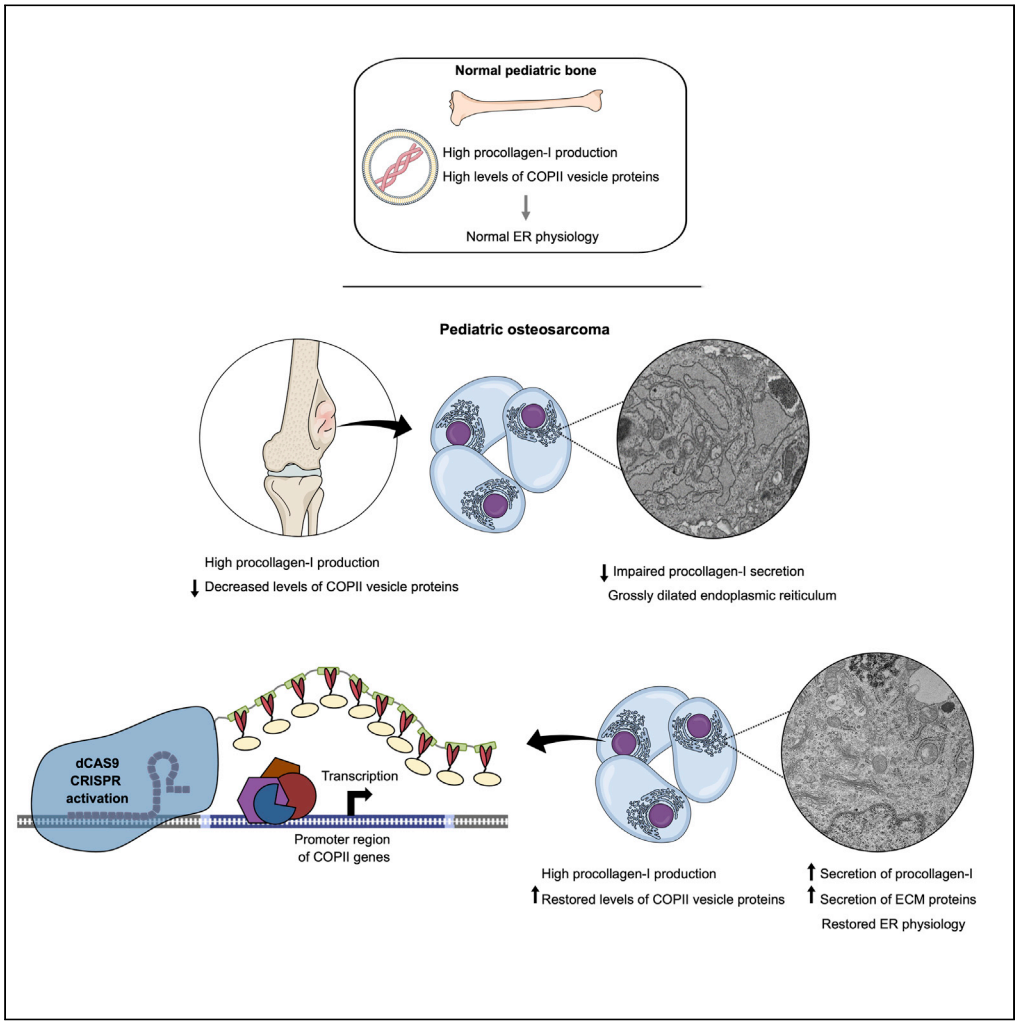

Rachael K. Wood, Ashley R. Flory, Melissa J. Mann, Lindsay J. Talbot, Linda M. Hendershot

linda.hendershot@stjude.org

Highlights

Exceptionally dilated ER is a conserved feature of genetically variable osteosarcomas.

Data from 108 pediatric OS reveal a widespread downregulation of 4 COPII components.

COPII insufficiency reduced secretion of collagen and extracellular matrix proteins.

Reexpression of SAR1A and SEC24D was sufficient to restore ER morphology.

Wood et al., iScience 25, 104100
April 15, 2022
https://doi.org/10.1016/j.isci.2022.104100

iScience

CellPress
OPEN ACCESS

Article

Secretory defects in pediatric osteosarcoma result from downregulation of selective COPII coatomer proteins

Rachael K. Wood,[1,3] Ashley R. Flory,[1] Melissa J. Mann,[1] Lindsay J. Talbot,[2] and Linda M. Hendershot[1,3,4,*]

SUMMARY

Pediatric osteosarcomas (OS) exhibit extensive genomic instability that has complicated the identification of new targeted therapies. We found the vast majority of 108 patient tumor samples and patient-derived xenografts (PDXs), which display an unusually dilated endoplasmic reticulum (ER), have reduced expression of four COPII vesicle components that trigger aberrant accumulation of procollagen-I protein within the ER. CRISPR activation technology was used to increase the expression of two of these, *SAR1A* and *SEC24D*, to physiological levels. This was sufficient to resolve the dilated ER morphology, restore collagen-I secretion, and enhance secretion of some extracellular matrix (ECM) proteins. However, orthotopic xenograft growth was not adversely affected by restoration of only *SAR1A* and *SEC24D*. Our studies reveal the mechanism responsible for the dilated ER that is a hallmark characteristic of OS and identify a highly conserved molecular signature for this genetically unstable tumor. Possible relationships of this phenotype to tumorigenesis are discussed.

INTRODUCTION

Osteosarcoma (OS) is a high-grade, malignant tumor and the most common pediatric bone tumor (Durfee et al., 2016). Primary disease most often occurs at the metaphysis of the distal femur, proximal tibia, or proximal humerus during periods of rapid bone growth in children and adolescents. The current treatment of OS is a combination of conventional antineoplastic neoadjuvant therapies and tumor resection surgery, followed by additional adjuvant chemotherapy. This regimen results in a 5-year survival rate of 65–70% for individuals presenting with localized tumors but less than 29% for those with recurrent or metastatic OS at the time of diagnosis (Isakoff et al., 2015; Meazza and Scanagatta, 2016). Advances in limb salvage surgery have improved the quality of life for individuals with OS; however, there has been little progress in survival rates over the last three decades.

Whole genome sequencing of pediatric tumors has led to the identification of conserved molecular changes in a number of cancers, providing targets for new treatment strategies. However, OS is characterized by extreme chromosomal instability and gene copy number variations, resulting in genetic heterogeneity and diversity across tumors (Lorenz et al., 2016; Martin et al., 2012; Chen et al., 2014). This striking variability has prevented the identification of a conserved molecular etiology for OS, other than extreme genomic instability. Instead, tumorigenesis appears to be the result of several different driver mutations and altered signaling pathways that synergistically combine to produce these aggressive and genetically complex tumors (Rickel et al., 2017; Moriarity et al., 2015). Mutations in both TP53 and RB1 are common among all types of sporadic OS (Moriarity et al., 2015), and the use of genetically engineered mouse models and patient-derived xenograft (PDX) studies underscore the role of TP53 in OS tumor suppression. Molecular characterization of patient tumors also identified activation or increased expression of several oncogenes including *C-FOS*, *C-JUN*, and *C-MYC*, as well as disruptions in a number of signaling pathways like PI3K, MAPK, and ErbB in individual tumors arguing for their contribution to OS tumorigenesis (Kansara et al., 2014; Moriarity et al., 2015; Weekes et al., 2016).

For all histological subtypes of OS, the presence of unmineralized bone matrix osteoid is a requirement for the diagnosis of OS (Mutsaers and Walkley, 2014; Misaghi et al., 2018). Osteoid is composed of 94% collagen, with collagen-I comprising the predominant subtype. Like all collagens, collagen-I is synthesized

[1]Department of Tumor Cell Biology, St. Jude Children's Research Hospital, Memphis, TN 38105, USA

[2]Department of Surgery, St. Jude Children's Research Hospital, Memphis, TN 38105, USA

[3]University of Tennessee Health Science Center, Memphis, TN 38163, USA

[4]Lead contact

*Correspondence: linda.hendershot@stjude.org

https://doi.org/10.1016/j.isci.2022.104100

in the endoplasmic reticulum (ER) from the procollagen precursor, which is composed of two COL1A1 and one COL1A2 subunits (Gelse et al., 2003). Procollagen chains enter the ER co-translationally where they undergo multiple posttranslational modifications and are assembled into rigid helical trimers that are 300–400 nm in length. Like all secretory pathway cargo, procollagen is subjected to ER quality control (ERQC) measures that monitor its folding, assembly, and posttranslational modifications. After passing ERQC, procollagen trimers are transported to the Golgi apparatus and subsequently assembled into the extracellular matrix (ECM). However, conventional COPII vesicles have defined geometries that are too small to accommodate procollagen. Instead, nonconventional structures are formed to traffic this unusually large and rigid cargo (Gorur et al., 2017; Raote and Malhotra, 2021).

Despite the genetic diversity among OS tumors, the single unifying feature identified in OS is an extremely dilated ER observed by electron microscopy. This abnormal phenotype is unique to OS (Williams et al., 1976; Aparisi et al., 1982; Steiner et al., 2006) and is conserved in pediatric OS tumors and their corresponding PDXs (Stewart et al., 2017). To understand the significance of this aberrant phenotype for OS, we used a combination of RNA-seq data derived from 108 patient tumors (Zhou et al., 2016), 2 OS PDXs and 3 OS cell lines, coupled with biochemical and cell biological assays. We identified a highly conserved decrease in the expression of four critical COPII gene transcripts relative to their levels in normal osteoblast tissue and lines. This correlated with the retention of collagen-I within the ER and led to the abnormal ER morphology that is characteristic of OS tumors. Using the nuclease deficient dCas9-SunTag-VP64 system (Tanenbaum et al., 2014), we found that restoration of only two of these COPII proteins, SAR1A and SEC24D, to levels observed in normal osteoblasts, was sufficient to restore collagen-I secretion and relieve the abnormal ER dilation. This decrease in expression of a subset of COPII transcripts and proteins may represent a uniform molecular signature for pediatric OS tumors.

RESULTS

Procollagen accumulates in the dilated ER of osteosarcomas

A number of OS patient-derived xenograft (PDX) tumors have been established at SJCRH and undergone in-depth genetic analyses (Stewart et al., 2017). When these PDXs are grown in mice using an orthotopic model, the resulting tumors from all 13 PDXs possess a grossly dilated ER that is characteristic of OS patient tumor samples (Figure 1A). Ultrastructural examination reveals the electron dense material within the dilated ER consistent with the presence of protein, most of which is expected to represent procollagen. In keeping with this, we found OS PDXs expressed high levels of both *COL1A1* and *COL1A2* collagen transcripts, which were similar to those in normal osteoblast tissues (Figure 1B).

The SJCRH OS PDXs have not been adapted to tissue culture, thus limiting the biochemical and cell biological assays available to characterize their ER defect. Therefore, to begin with a more experimentally tractable system that could be used to guide subsequent studies with PDX and patient tumors, we obtained three commonly used OS cell lines as well as a pre-osteoblast cell line as a control. Examination of these lines using transmission electron microscopy revealed that the pre-osteoblast line hFOB1.19 possessed a normal ER morphology (Figure 1C) similar to that observed in healthy osteoblast tissue. Hence, the abundant production of collagen-I by osteoblasts does not distort the ER, implying instead that the abnormal ER phenotype is specific to malignant osteosarcoma cells. Examination of three commonly used OS cell lines revealed that only the SaOS2 line possessed the dilated ER morphology that is uniformly characteristic of OS patient tumors and PDXs (Figure 1D), whereas 143B (Figure 1E) and U2OS (data not shown) cells had a normal ER morphology. RNA expression data revealed that SaOS2 cells expressed both procollagen-I transcripts at levels similar to those in the osteoblast line, whereas *COL1A1* and *COL1A2* transcripts were expressed at negligible levels in U2OS and 143B cells (Figure 1B). This suggested that the two OS cell lines lacking an abnormal ER had incurred additional genetic alterations that limited collagen gene expression.

Low levels of ER stress leading to activation of a homeostatic unfolded protein response (UPR) play a key role in normal osteoblast differentiation (Murakami et al., 2009; Horiuchi et al., 2016), and UPR activation is also observed in many solid tumors and cell lines because of their high metabolic rate and insufficient environment (reviewed in (Oakes, 2020)). We explored whether the dilated ER observed in OS indicated a particularly robust or abnormal UPR. RNA-seq data from the two PDXs and three OS lines revealed that activation of downstream targets of all three UPR branches was comparable to that observed in the corresponding osteoblast control tissues (Figure S1A). This does not represent maximal UPR

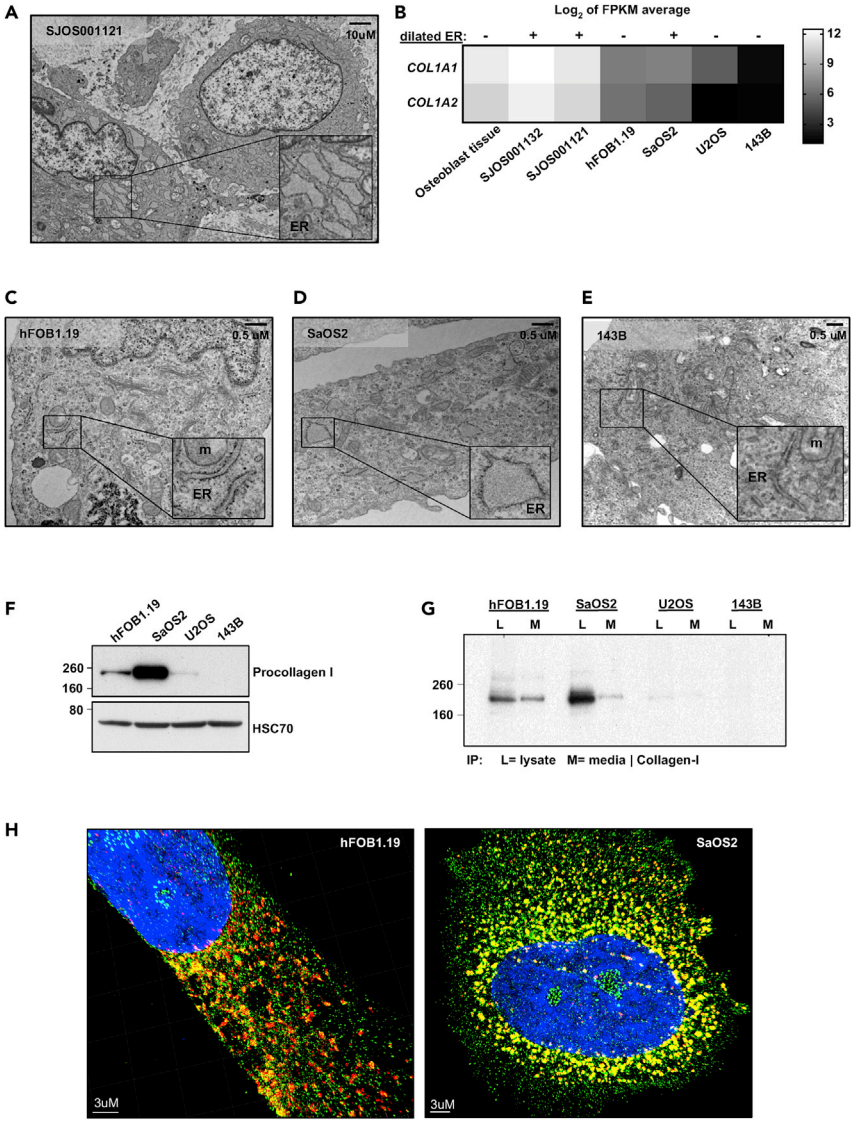

Figure 1. Collagen I is retained in the ER in an OS cell line that phenocopies the grossly dilated ER associated with patient tumors

(A) Transmission electron microscopy images were obtained of an OS xenograft (PDX) derived from an SJCRH patient tumor, which revealed the same dilated ER phenotype as has been observed in primary tumors. The inset shows an enlargement of the ER.

(B) The heatmap is a representation of the log2 values of averaged FPKM reads acquired from RNA-seq analyses for *COL1A1* and *COL1A2* transcripts (cell lines, n = 3 independent replicates). Expression data from normal osteoblast tissue and two SJCRH PDXs are on the left followed by hFOB1.19, an osteoblast cell line, and three OS tumor cell lines. Each sample is annotated above the expression data as having a normal (–) or dilated (+) ER morphology.

(C–D) EM images of the cell lines used include: (C) hFOB1.19, a human osteoblast cell line possessing a normal ER, (D) SaOS2, an OS cell line with a dilated ER, and (E) 143B, an OS cell line that exhibits normal ER morphology.

(F) Western blot analysis of cell lysates from the indicated cell lines probed for collagen-I (anti-SP1.D8), and HSC70 provided as a loading control.

(G) Cell lines were metabolically labeled for 16 h and both culture media (M) and cell lysates (L) were immunoprecipitated with anti-SPI.D8 monoclonal and analyzed by reducing SDS-PAGE.

(H) Super-resolution structured illumination microscopy was used to examine hFOB1.19 and SaOS2 cells, which revealed procollagen-I expression was limited to the ER in SaOS2 cells relative to its expression outside the ER in hFOB1.19 osteoblasts. The cells were immunostained for ER luminal protein GRP170 (green) and procollagen-1 (anti-SP1.D8, red). The (yellow) is an overlay of procollagen-I and GRP170 staining. The nucleus was visualized with a DAPI stain (blue).

activation, as treatment of all three OS cell lines with thapsigargin, a chemical ER stress inducer, resulted in further increases of downstream targets (Figures S1B and S1C). Furthermore, RNA expression data from 108 pediatric OS patient tumors deposited in the Pediatric Cancer (PeCan) database revealed UPR target transcripts were expressed at similar or lower levels than those observed in non-transformed osteoblast tissue (Figure S1D). Thus, unduly high levels of ER stress were not responsible for the abnormal ER ultrastructure associated with OS.

SaOS2 cells with dilated ER exhibit reduced collagen-I secretion

Although the SaOS2 tumor line, which possessed a dilated ER phenotype, and the hFOB1.19 osteoblast line produced equivalent amounts of both collagen-I transcripts (Figure 1B), examination of corresponding cell lysates revealed much higher levels of procollagen-I protein in SaOS2 cells (Figure 1F). To establish if there was a defect in protein secretion from the OS cells, we metabolically labeled the hFOB1.19 and SaOS2 cell lines and immunoprecipitated collagen-I from both the cell lysates and culture media. Although both cell lines produced type I procollagen subunits at similar levels, the osteoblast line readily secreted it, whereas procollagen produced in SaOS2 cells remained largely cell associated (Figure 1G). In keeping with the very low levels of procollagen transcripts present in U2OS and 143B cells, procollagen protein was extremely low as determined by both western blot and metabolic labeling (Figures 1F and 1G). Analysis of the SaOS2 cell line using super-resolution structured illumination microscopy revealed procollagen-I staining completely overlapped with that of the ER marker GRP170, indicating that procollagen-I was accumulating within the globular shaped ER of SaOS2 cells (Figure 1H). In contrast, similar examination of hFOB1.19 cells detected a pool of procollagen that co-stained with GRP170, as well as a population that did not, because of its trafficking further along the secretory pathway (Figure 1H). Together, this indicates that the defect in procollagen-I secretion is because of abnormal ER retention, which contributes to the electron dense material observed within the dilated ER of OS.

Decreased expression of a subset of COPII transcripts in OS tumors and cell lines

The absence of UPR activation beyond basal levels present in osteoblasts suggested that the defect in collagen secretion was unlikely to represent a problem with collagen folding or assembly in the ER. Once the secretory cargo has matured properly and passed ER quality control measures, it is transported from the ER to the Golgi via COPII-containing structures. This occurs at ER exit sites and is initiated when the GTP-bound form of SAR1 inserts into the cytosolic leaflet of the ER membrane, which is followed by the assembly of an inner coat composed of SEC23:SEC24 heterodimers and an outer coat of SEC13:SEC31 heterotetramers. The rigid procollagen trimers that assemble in the ER are ~300-400nM in length, and therefore cannot be accommodated by conventional COPII transport structures. Although they still rely on COPII components to reach the Golgi, this requires two additional proteins, TANGO1 and cTAGE5. These specialized proteins bind procollagen at ER exit sites and assist in the distortion of COPII vesicle formation. Initially they were thought to allow the synthesis of mega-carrier vesicles (Raote et al., 2018; Gorur et al., 2017; Yuan et al., 2018); however, more recent studies argue instead that these proteins help form tubular structures emanating from the ER, which allow procollagen to more directly be delivered to the Golgi (Raote and Malhotra, 2021, Mccaughey et al., 2019). To determine if cargo recognition or vesicle assembly was defective, we examined transcript levels of the 22 possible proteins involved in the formation of COPII vesicles for transporting procollagen. We found that TANGO1 and cTAGE5 transcripts were expressed at normal levels in the OS lines, PDX tumors, and patient tumors compared to the appropriate controls (Table S1). Thus, neither recognition of the procollagen triple helices for packaging nor the ability to alter the COPII structures to accommodate this rigid cargo appeared to be defective.

We also examined the expression of the multiple proteins and their corresponding isoforms that produce COPII vesicles. RNA-seq was performed on two OS-PDXs and three OS cell lines, and the resulting data was normalized to their respective control tissues. This revealed that mRNA levels for most COPII components were very similar to those found in their respective normal controls. However, the following six COPII genes, *SAR1A*, *SAR1B*, *SEC23A*, *SEC23B*, *SEC24A*, and *SEC24D*, exhibited a reduced expression based on RNA-seq data (Figure 2A and Data S1). Each of these COPII components belongs to a family with multiple members, which provides some specificity for cargo inclusion into the COPII vesicles. To determine if this trend was representative of patient tumors, we compared RNA expression data available for 108 pediatric OS tumors in the pediatric cancer (PeCan) database to normal human osteoblast tissue. This analysis revealed a decreased expression of four of these six COPII components in patient tumors, which included

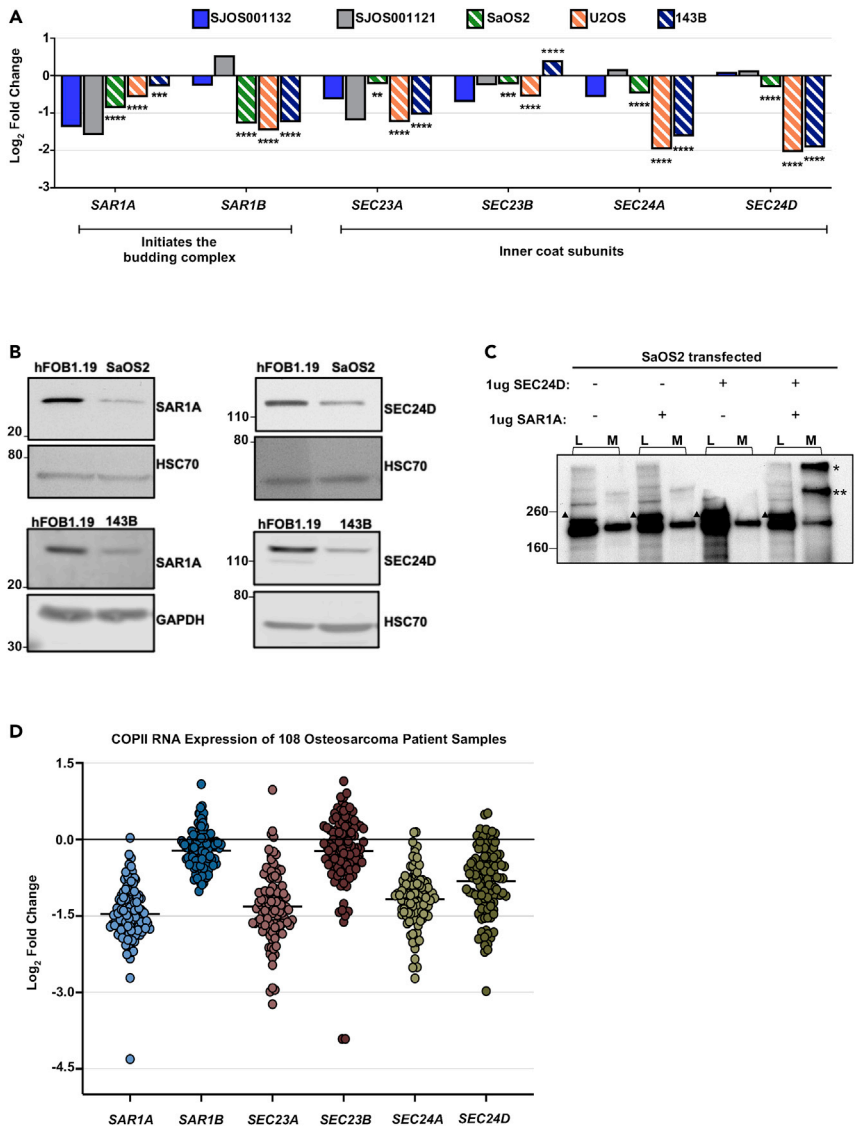

Figure 2. OS, PDXs, and cell lines have reduced levels of a subset of COPII vesicle components

(A) RNA-Seq analyses of the indicated COPII component transcripts from two SJCRH PDX tumors (solid bars) normalized to normal human osteoblast tissue samples. RNA seq data from the indicated OS cell lines (striped bars) were averaged and normalized to hFOB1.1 9 (n = 3 biological replicates). **P ≤ 0.01, ***P ≤ 0.001 and ****P ≤ 0.0001

(B) Cell lysates from the indicated cell lines were examined by western blot analyses for SAR1A and SEC24D expression. HSC70 or GAPDH are included as loading controls.

(C) SaOS2 cells were transfected with 1 μg of *SEC24D* and *SAR1A* expression constructs either individually or in combination. 48 hrs post-transfection cells were metabolically labeled for 16 h. Both cell lysates (L) and culture supernatant (M) were immunoprecipitated with anti-collagen-I serum (anti-SP1.D8) and analyzed by reduced SDS-PAGE. The mobility of procollagen monomers (▲) in the cell lysates is labeled, as are collagen trimers (*) and dimers (**) in the media.

(D) The scatter plot displays the log2 fold change of six COPII transcripts from 108 OS patient tumor samples compared to normal osteoblast tissue. The (black) midline bar indicates the mean value for the tumor samples.

SAR1A, SEC23A, SEC24A, and *SEC24D* with respective log2 fold changes of −1.5, −1.3, −1.2, and −0.8 (Figure 2D). Unlike the OS cell lines, levels of *SAR1B* and *SEC23B* were not consistently reduced. Similar to the OS cell lines and PDXs, the remaining 18 COPII genes were largely unchanged. These data suggested a possible cause for the abnormal ER phenotype that is a hallmark of OS tumors and revealed a molecular signature encompassing the majority of OS tumors despite their high degree of intra-tumor and inter-tumor genetic heterogeneity.

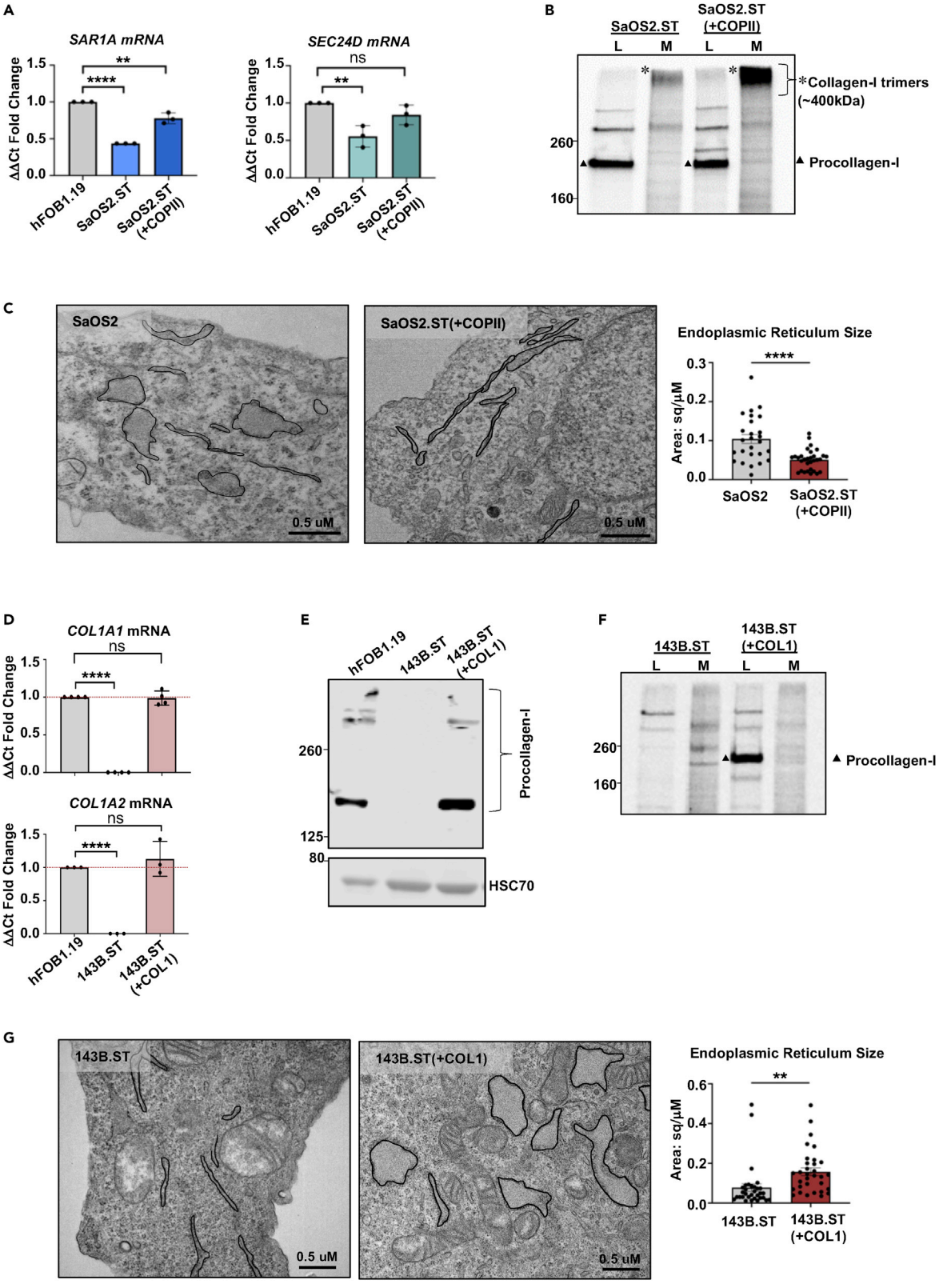
A
SAR1A mRNA
ΔΔCt Fold Change
1.5
1.0
0.5
0.0
**
****
hFOB1.19
SaOS2.ST
SaOS2.ST (+COPII)
SEC24D mRNA
ns
**
B
SaOS2.ST
(+COPII)
L
M
*Collagen-I trimers (~400kDa)
Procollagen-I
260
160
C
SaOS2
SaOS2.ST(+COPII)
0.5 uM
Endoplasmic Reticulum Size
Area: sq/μM
0.3
0.2
0.1
0.0
****
SaOS2
SaOS2.ST (+COPII)
D
COL1A1 mRNA
ns
****
COL1A2 mRNA
143B.ST
143B.ST (+COL1)
E
hFOB1.19
143B.ST
143B.ST (+COL1)
Procollagen-I
260
125
80
HSC70
F
143B.ST
143B.ST (+COL1)
Procollagen-I
260
160
G
143B.ST
143B.ST(+COL1)
0.5 uM
Endoplasmic Reticulum Size
0.6
0.4
0.2
0.0
**

Figure 3. Swollen ER associated with OS is caused by a combination of collagen I synthesis and a defect in COPII expression

(A) *SAR1A* and *SEC24D* mRNA transcripts from SaOS2.ST and SaOS2.ST(+COPII) cells were analyzed by qRT-PCR and normalized to their values in hFOBI.19 cells (n = 3). The difference in values between SaOS2.ST and the osteoblast line were significant to $p \leq 0.0001$ for *SAR1A* (****) and $p \leq 0.01$ for *SEC24D* (**), whereas the restored values for *SEC24D* were not significantly different (ns) than those of the hFOB1.19 cell line. *SAR1A* expression was increased in the SaOS.ST(+COPII), but it did not quite reach that of the control osteoblast line.

(B) The indicated cell lines were metabolically labeled for 16 h, and culture media and cell lysates were harvested. Procollagen-1 (▲) was isolated from the cell lysates (anti-M-38), and collagen-1 (*) was immunoprecipitated from the media (anti-collagen-I #ab34710) and analyzed by reduced SDS-PAGE (n = 3 biological replicates).

(C) Cells were examined by transmission electron microscopy, and images were analyzed using ImageJ software. ER membranes were traced, and the area measured was based on image calibration (n = 4-5 individual cells per cell line with 26–31 total ER regions quantified for each line). Differences between the two lines were computed using unpaired two-tailed Student's t-tests and were calculated to be $p \leq 0.0001$ (****).

(D) *COL1A1* and *COL1A2* mRNA was obtained from hFOB1.19, 143B.ST, and 143B.ST(+COL1) cell lines and quantified by qRT-PCR. Transcript levels are expressed relative to those in hFOB1.19 (n = 3 independent replicates). ns: not significant, ****$P \leq 0.0001$.

(E) Western blot analysis of procollagen-I expression (anti-SP1.D8) in the lysates of indicated lines. HSC70 served as a loading control.

(F) Cells were metabolically labeled for 16 h; procollagen-I (▲) was isolated from cell lysates (L) with anti-M-38, and collagen-I was immunoprecipitated from the culture supernatant (M) with anti-[COLI] #ab90395. Isolated material was analyzed by reducing SDS-PAGE (n = 3 biological replicates).

(G) Transmission electron micrographs of 143B.ST and 143B.ST(+COL1) cells were analyzed in Image J software. ER membranes were traced and measured based on image calibration (n = individual cells per cell line were examined with 32 total ER regions measured in each line). Statistical differences between the two lines were computed as in (C) and calculated to be significant to $p \leq 0.01$ (**). All error bars indicate mean ± SD.

Restoring SAR1A and SEC24D expression in SaOS2 cells is sufficient to enhance collagen-I secretion and rescue abnormal ER phenotype

A previous study employed siRNA to reduce the expression of 18 of the COPII components to identify those required to transport procollagen-I. Only 8 of these proteins reduced collagen-I secretion by at least 50% when targeted individually (Maiers et al., 2017). SAR1A and SEC24D were among those required, whereas decreased expression of SEC23A or SEC24A did not significantly impact collagen secretion when downregulated alone. This suggested that restoring the expression of only SAR1A and SEC24D might be sufficient to both rescue collagen secretion and establish normal ER morphology. To assess if this might be the case, we transiently expressed *SAR1A* and *SEC24D* constructs in the SaOS2 cell line alone and together and observed an increase in collagen-I secretion when both were co-expressed (Figures 2B and 2C). To determine methods amenable to provide stable restoration of *SAR1A* and *SEC24D* expression, we exploited the fact that in-depth, genome-wide transcriptional analyses were available on pediatric OS-PDX tumors (Stewart et al., 2017) and found that epigenetic silencing of these genes was not responsible for the reduction in COPII transcript levels (Figures S2A and S2B).Because both *SAR1A* and *SEC24D* were transcriptionally active, we chose the nuclease deficient dCas9-SunTag-VP64 system (Tanenbaum et al., 2014) to restore expression from their endogenous promoters. This multicomponent system uses an enzymatically inactive Cas9 protein (dCas9) that is fused with a 10× peptide repeat, which acts to recruit intrabody proteins fused to the strong transcriptional activator, VP64. SaOS2 cells were transduced with lentiviruses modified to express the various SunTag components to obtain a parental line SaOS2.ST, which was subsequently used to introduce single guide RNAs (sgRNAs). Ten gRNAs targeting each of the promoter regions of *SAR1A* and *SEC24D* were tested independently for their ability to increase the expression of these proteins to a level as close as possible to that observed in the osteoblast cell line, hFOB1.19. Based on this criterion, one gRNA was chosen for each of the two genes and engineered into the dual sgRNA expression cassette. Stable bulk cell lines were selected for puromycin resistance, which we referred to as SaOS2.ST(+COPII) for brevity, even though only two of the four under-expressed COPII components were restored (Figure S3).

Examination of *SAR1A* and *SEC24D* transcripts and protein in SaOS2.ST(+COPII) cells revealed they were expressed at levels similar to those observed in the normal bone cell line, hFOB1.19 (Figures 3A and S5), although *SAR1A* expression did not quite reach that of the control line. After metabolic labeling, cell lysates and culture media from both lines were immunoprecipitated with anti-procollagen-I or anti-collagen-I, respectively. Significantly greater amounts of large collagen trimers were readily isolated from the culture supernatant of the SaOS2.ST(+COPII) cells compared to that of the parental SaOS2.ST line, indicating that restoring only SAR1A and SEC24D levels was sufficient to increase collagen-I protein transport from the ER leading to its secretion (Figure 3B). Both cell lines were additionally subjected to electron microscopy, and ImageJ software was used to quantify ER area. Relative to cells without sgRNA expression, SaOS2.ST(+COPII) cells displayed a significant reduction in ER area that possessed a more typical morphology (Figure 3C). Together, these data demonstrate that decreased COPII protein levels in OS caused ER retention of collagen-I protein and resulted in a gross dilation of this organelle. Restoring levels

of SAR1A and SEC24D protein expression led to increased collagen-I secretion and normalization of the dilated ER morphology associated with OS.

Reexpression of COL1A1 and COL1A2 in COPII-deficient 143B cells results in a block in collagen-I secretion and ER dilation

Levels of both *SAR1A* and *SEC24D* were reduced in the 143B OS cell line (Figures 2A and 2B), even though the ER morphology was normal. However, unlike SaOS2 cells, the PDXs, and the 108 patient tumor samples, 143B cells did not produce collagen-I (Figures 1B–3D). To confirm that ER dilation was caused by a combination of both normal collagen-I expression and a decrease in COPII transcripts, we introduced the dCas9-SunTag-VP64 system into these cells, which are hereby referred to as 143B.ST cells (Figure S3). Next, sgRNAs targeting the *COL1A1* and *COL1A2* promoters were selected based on their ability to establish transcript levels similar to that of the normal bone cell line hFOB1.19. A bulk culture, referred to as 143B.ST(+COL1), was obtained, and *COL1A1* and *COL1A2* transcripts were found to be comparable to those in the hFOB1.19 line (Figure 3D). After normalizing to the loading control, steady state procollagen protein levels were found to be slightly higher in 143B.ST(+COL1) cells compared to the normal osteoblast line (Figure 3E). To determine if this might represent a defect in the ability to secrete collagen-I, the 143B.ST and 143B.ST(+COL1) cells were metabolically labeled, and procollagen-I and collagen-I were isolated from cell lysates and culture media, respectively (Figure 3F). Although procollagen-I was readily detected in the lysate of cells expressing the sgRNAs specific to *COL1A1* and *COL1A2*, there was no evidence that collagen-I was being secreted from these cells in the absence of normal COPII levels. We examined electron micrographs to determine the effect of collagen-I retention on the ER morphology of 143B.ST(+COL1) cells. Images revealed that the collagen-I-engineered 143B variants contained a significantly distended ER morphology that was comparable to that associated with OS patient tumors (Figure 3G). These data demonstrate the abnormal ER morphology that is a hallmark of OS is a result of reduced expression of a subset of COPII proteins in combination with normal collagen-I expression. Together, this causes procollagen-I to be retained in the ER and results in ER dilation. To our knowledge, the uniform decrease in expression of this subset of COPII complex genes represents the first conserved molecular signature for osteosarcomas, other than genomic instability.

To further characterize the effects of COPII deficiency on OS biology, we restored SAR1A and SEC24D levels in 143B.ST cells using sgRNAs similar to that of SaOS2 cells. We reasoned the absence of collagen production in the 143B OS line might increase our ability to detect changes in secretion of less abundant proteins. Spectral count data revealed a total of 234 proteins showed a significant increase in the culture supernatant of 143B.ST(+COPII) cells compared to 143B.ST cells with p values of <0.05, and 162 of these proteins met a cut-off p value of <0.01 (red) (Figure 4B and Data S2). The latter group was analyzed using the Gene Ontology database, QuickGO, to identify their normal subcellular location (Figure 4C). Only 29 of these were proteins that enter the ER co-translationally, and a sizable portion of them were resident ER proteins that are not usually secreted. However, tumor cells have been reported to express ER chaperones on their cell surface or to secrete them (Van Krieken et al., 2021). The small number of secreted proteins that were affected by COPII restoration is compatible with previous studies reporting that reducing expression of SAR1A or SEC24D has negligible effects on the transport of most secretory pathway proteins (Cutrona et al., 2013; Sarmah et al., 2010). Conversely, the large proteins that comprise the ECM are more dependent on the noncanonical mechanism of transport from the ER used by collagen, and *Sec24D* mutations in zebrafish led to a severely diminished ECM (Cutrona et al., 2013; Sarmah et al., 2010). Accordingly, our proteomics data revealed a modest increase in the secretion of several ECM components from the 143B.ST(+COPII), including laminin, TGFβ-induced protein ig-h3, metalloprotease inhibitors 1 and 2 (TIMP1 and 2), and both thrombospondin −1 and −2 (TSP-1/2) (Data S2). Using western blot analyses, we verified the increased secretion of one of them, TIMP1, from the 143B.ST(+COPII) cells (Figure 4D). Unexpectedly, the majority of proteins that were increased in the culture supernatant after COPII restoration are the ones that are usually localized to intracellular compartments. It is noteworthy that 79% of these have previously been identified in exosomes or other extracellular vesicles (Zhang and Yu, 2019; Mathivanan et al., 2012), indicating a possible unreported link between these two COPII proteins and extracellular vesicle secretion. The secretion of one of these, vimentin, was examined by western blotting, which revealed it to be increased in the culture supernatant of 143B.ST(+COPII) cells (Figure 4D).

Decreased COPII expression does not provide a benefit to OS invasion or tumorigenesis

Having identified the cause of the abnormal ER morphology and corrected the phenotype, we wished to determine if decreased expression of SAR1A and SEC24D was beneficial to OS tumorigenesis. We considered two

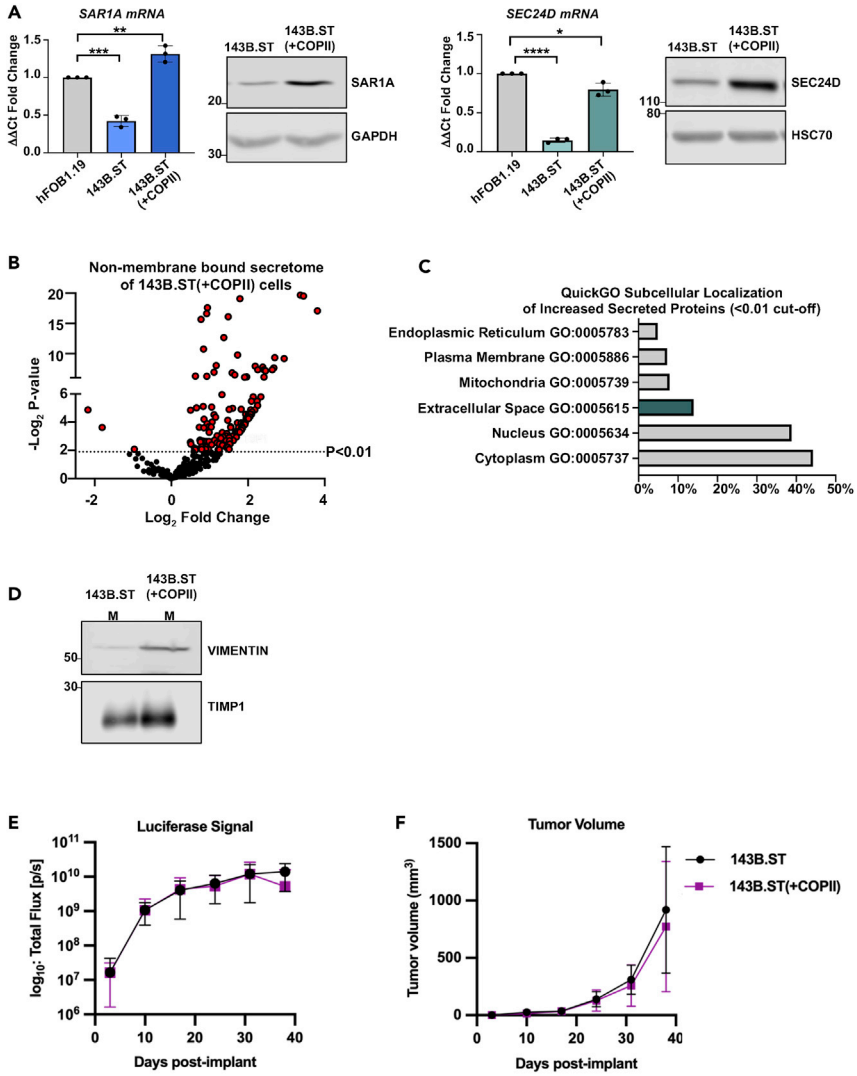

Figure 4. COPII insufficiency affects secretion of ECM proteins, but restoration of only SAR1A and SEC24D does not appear to adversely affect growth in orthotopic xenograft model

(A) *SAR1A* and *SEC24D* mRNA transcripts from 143B.ST and143B.ST(+COPII) cells were analyzed by qRT-PCR and expressed relative to their values in hFOBl.19 cells (n = 3). The differences in values for 143B.ST and the osteoblast line were significant to $p \leq 0.001$ for *SAR1A* (***) and $p \leq 0.0001$ for *SEC24D* (****). The restored values were greater than that of the hFOB1.19 for *SAR1A* $p \leq 0.01$ (**) and slightly less for *SEC24D* $p \leq 0.05$ (*). Error bars indicate mean $\pm$ SD.

(B) Spectral counts were transformed to log2 and averaged (n = 2 biological replicates) and fold change calculated. Fold change values were plotted against the -log10 of the p value with all significant hits of $p \leq 0.01$ indicated (red). The p values were derived by G-test.

(C) Uniprot IDs of significantly, differentially expressed proteins were analyzed using QuickGO for subcellular location determination.

(D) Cells were cultured in serum free media for 20 h and secreted proteins were TCA-precipitated, followed by Western blot analysis with anti-TIMP1 and anti-vimentin.

(E) 100K cells of 143B.ST or 143B(+COPII) were implanted into the right tibia of CD1-nude mice (n = 10 for each line). On day 3 postimplantation, the luciferase signal was measured and then every 7 days thereafter to monitor tumor growth. Total bioluminescence flux of the region of interest (right tibia) was plotted against days postimplant.

(F) Caliper measurements were recorded to supplement luciferase imaging, and tumor volume calculated.

Statistical differences between both the luciferase signal and tumor volume for 143B.ST and 143B.ST(+COPII) cells were computed using unpaired, two-tailed Student's t-tests for each time point comparison and group overall and were discovered to be nonsignificant. All error bars indicate mean $\pm$ SD.

hypotheses: first, it was possible that reducing the secretion of collagen might be advantageous; second, to test this, the pair of SaOS2 lines would prove useful. Alternatively, although preventing collagen secretion was responsible for the conserved phenotype, it was possible that the critical target of COPII-insufficiency was another secretory pathway protein(s), component of the ECM, and/or extracellular vesicles. The two 143B lines would be useful for testing the latter hypothesis and were particularly appealing because of their high tumor take rate and metastatic potential (Luu et al., 2005). Proliferation rates for both lines were unaffected by COPII restoration (Figure S4A). Their invasion capability was tested using an *ex vivo* collagen invasion assay. Restoration of SAR1A and SEC24D had no effect on SaOS2 invasion, and although invasion of the restored 143B line was slightly impaired compared to that of its parental line, this difference was not statistically significant (Figure S4B). To test the effects of SAR1A and SEC24D restoration in an *in vivo* model, we used the 143B.ST(-/+COPII) cells in an improved method for establishing orthotopic xenograft tumors (Talbot et al., 2021). Tumors were detected by fluorescence imaging in all 10 mice in both experimental groups 3 days following implantation, revealing tumor take rates were not affected by COPII restoration (Figure S4C). Thereafter, tumor growth was examined weekly by fluorescence imaging, and the tumor mass was measured using calipers. There was no significant difference in the growth rate or size of the COPII-deficient compared to the COPII-restored 143B line (Figures 4E and 4F), and a single mouse from each group developed a lung metastasis during the course of the experiment. Furthermore, the growth rate of both lines was similar to that reported for the parental unmodified 143B (Yuan et al., 2009) line. Tumors obtained from each experimental group were analyzed for *SAR1A*, *SEC24D*, *COL1A1*, and *COL1A2* transcripts. In all cases, the genetic changes we introduced in the lines were present in the tumors that grew out and neither of the 143B lines synthesized collagen after *in vivo* growth (data not shown).

DISCUSSION

In spite of the molecular variability between tumors and even within individual tumors, an unusually dilated ER has been a highly conserved feature OS (Williams et al., 1976; Aparisi et al., 1982) and was observed in all 13 PDX tumors examined in a recent study (Stewart et al., 2017). We reasoned that understanding the underlying cause of this phenotype might provide an elusive molecular signature for pediatric OS. By analyzing genomic data from 108 OS tumors, two OS PDXs, and three OS cell lines, we found four COPII components; *SAR1A*, *SEC23A*, *SEC24A*, and *SEC24D*, were expressed at lower levels than those found in normal osteoblast tissues, and that this decrease in a subset of COPII proteins was responsible for the characteristic OS phenotype. In the past several years, significant progress has been made in our understanding of client specificity among the various COPII components, as well as the mechanism of transporting large, rigid clients like collagen and ECM components to the Golgi (Raote and Malhotra, 2021). In addition to requiring specialized cargo receptors like TANGO1and cTAGE5, large amounts of conventional COPII components are also needed to produce the tubular structures that deliver collagen to the Golgi. In fact, it has been estimated that their production is particularly reliant on abundant amounts of SAR1, SEC23, and SEC24 proteins to extend the inner layer of the growing ER bud (Ma and Goldberg, 2016). Therefore, the very proteins that are most required to form the tubular structures that transport collagen are downregulated in osteosarcoma. Although four COPII proteins were consistently downregulated in OS tumors, we found that restoring only SAR1A and SEC24D expression was sufficient to allow collagen secretion and prevent dilation of the ER. It is noteworthy that restoration of SEC23A in the OS line was not required for collagen transport, despite the experimental evidence showing that TANGO1 binds directly to SEC23A in the SAR1A, SEC23A, and SEC24 complex, instead of binding to SEC24 like other cargo receptors (Saito et al., 2009 Raote and Malhotra, 2021).

It is hard to imagine why accumulating collagen in the ER to a point that this organelle becomes grossly deformed would be beneficial to OS. All 108 OS tumors expressed high levels *COL1A1* and *COL1A2* transcripts. Given the genetic instability associated with OS, it seems likely that a significant reduction in their levels would have occurred in at least some of the tumors, if decreasing collagen secretion was beneficial to OS tumorigenesis. Consistent with collagen retention not playing a critical role in OS, our COPII-restored SaOS2 cell line, which now secreted collagen, was indistinguishable from the non-restored line in an invasion assay. A second possibility we considered was that blocking transport of another COPII-dependent, secreted protein was the critical target for OS tumorigenesis. Our proteomic spectral count data revealed that secretion of several ECM components was modestly increased upon SAR1A and SEC24D restoration. TSP-1 and TSP-2 are large multi-domain glycoproteins that are often downregulated by oncogenes and upregulated by tumor suppressors like p53 (Volpert et al., 1995). Overexpression of TSP-1 in an osteosarcoma xenograft model-inhibited tumor growth (Jian et al., 2019) and TSP-1 peptide mimetics are being used to treat canine OS (Rusk et al., 2006). TIMP is also credited with roles in tumorigenesis, and two different microRNAs expressed in OS target TIMP to promote

invasion and metastasis (Chao et al., 2019; Zhang et al., 2019). However, our xenograft studies did not indicate that the modest increase in ECM component secretion observed in the SAR1A and SEC24D-restored cells was sufficient to affect tumor growth.

An unanticipated observation from our study was the large number of cytosolic and nuclear proteins that were observed in the culture supernatant when SAR1A and SEC24D expression was restored in the 143B OS cell line. Owing to the lack of targeting sequences, these proteins should not enter the ER where they could be packaged in COPII carriers. A number of these cytosolic proteins are often included in extracellular vesicles, which are a diverse group of membrane-enclosed structures that can contain proteins, lipids, mRNA, and miRNAs to act as mediators of intercellular communication (Zhang and Yu, 2019). Importantly, our culture supernatant was not fractionated to establish if these proteins were released in exosomes or some other type of extracellular vesicle. Based on our current understanding of the biogenesis of extracellular vesicles, it is not clear how COPII components would contribute to the extracellular transport of these cytoplasmic proteins. It is likely that their effects are indirect; however, given the critical role extracellular vesicles play in tumorigenesis and immune responses for a variety of cancers including osteosarcoma (Zhang et al., 2021), this finding warrants further investigation.

Finally, it is possible that the critical gene that contributes to OS is one that is co-regulated with these four COPII genes, and that the signature enlarged ER is simply an unintended consequence of sharing the same transcriptional activator(s). We discovered that the decreased expression of the COPII genes in OS was not because of epigenetic silencing but was instead caused by reduced transcription. The COPII genes are ubiquitously expressed and are critical to the transport of secretory pathway proteins from the ER to Golgi. As such, the multiple components needed to produce these transport vesicles might be expected to be co-regulated and tuned to the secretory load of the cell. However, there is some evidence for more surgical regulation of individual components. CrebA in *Drosophila* (Fox et al., 2010) and CREB3 in medaka fish (Ishikawa et al., 2017) control a number of components of the secretory pathway including *Sec23* and *Sec24*. Like the mammalian CREB3 family of proteins, they are both members of the bZip transcription factor family and are closely related to the UPR transducer ATF6. These transcription factors are synthesized as integral ER membrane proteins with the transcription factor domain oriented to the cytoplasm, which is liberated in response to ER stress. Unlike ATF6, mammalian CREB3 family members are more restricted in their tissue expression, with particularly high levels of CREB3L1 found in osteoblasts (Sampieri et al., 2019). *CREB3L1/OASIS* knockout mice have a severe osteopenia, and their osteoblasts possess a grossly dilated ER containing bone matrix proteins (Murakami et al., 2009) similar to the OS phenotype. Transient overexpression of CREB3L1 in nonsecretory HeLa cells led to broad upregulation of secretory pathway components, including *SEC23A*, *SEC24A*, *SEC24D*, and *SAR1A* (Fox et al., 2010). In terms of its significance to tumorigenesis, CREB3L1 was shown to be a metastasis suppressor in a rat mammary tumor model, and chip-on-chip analyses identified a number of genes that contribute to cancer development as targets (Mellor et al., 2013). Similarly, epigenetic silencing of *CREB3L1* is correlated with a more aggressive phenotype in human bladder and breast cancer (Ward et al., 2016; Rose et al., 2014). However, we found *CREB3L1* transcript levels in pediatric OS tumors to be comparable or higher than in normal osteoblast tissue (data not shown). Importantly, ER stress is required to release the transcription factor domain allowing it to traffic to the nucleus, but the execution of this critical processing event remains to be investigated in OS. Given the promising nature of this transcription factor, further experiments are warranted.

In summary, the particularly high genomic instability associated with OS tumors has precluded the identification of a unifying molecular signature, although a grossly dilated ER has long been a poorly understood hallmark of this tumor. Our studies demonstrated this abnormal phenotype was caused by a combination of collagen production, which places unusually high demands on the secretory machinery, and the reduced expression of four COPII genes essential for the secretion of large cargo, like collagen-I. This reduction in COPII transcripts was conserved in the majority of 108 OS tumor patient samples, 2 OS PDXs, and 3 OS cell lines. Restoring SAR1A and SEC24D protein levels was sufficient to increase collagen-I secretion and resolve the abnormal ER dilation observed in an OS cell line. Understanding the cause of COPII component downregulation and the significance of this phenotype to OS may identify potential vulnerabilities to exploit.

LIMITATIONS OF THE STUDY

There are a couple limitations to this study that should be considered. First, there were four COPII genes decreased in the majority of OS patient samples. However, here we only restored two, *SAR1A* and *SEC24D*.

Although these two proteins proved sufficient to increase collagen-I secretion and restore ER morphology, there is the possibility that restoring all four genes might be required for secretion of biologically effective quantities of anti-tumorigenic proteins. In addition, the fact that our studies were conducted in CD-1 nude mice did not allow us to examine possible effects of altered ECM on tumor immunity. Both caveats should be considered in future studies.

STAR★METHODS

Detailed methods are provided in the online version of this paper and include the following:

- KEY RESOURCES TABLE
- RESOURCE AVAILABILITY
  - Lead contact
  - Materials availability
  - Data and code availability
- EXPERIMENTAL MODEL AND SUBJECT DETAILS
  - Cells
  - Animals
- METHOD DETAILS
  - mRNA expression studies
  - Metabolic labeling experiments
  - Immunoblotting
  - Transmission electron microscopy
  - CRISPRa cloning using the SunTag system
  - Microscopy
  - Proliferation assay
  - Invasion assay
  - Proteomic analyses
- QUANTIFICATION AND STATISTICAL ANALYSIS
  - RNA expression studies
  - ER area measurement
  - Proliferation assay
  - Invasion assay
  - Proteomics statistics

SUPPLEMENTAL INFORMATION

Supplemental information can be found online at https://doi.org/10.1016/j.isci.2022.104100.

ACKNOWLEDGMENTS

We wish to thank Dr. Cam Robinson and Sharon Frase, along with the Cell and Tissue Imaging core for providing transmission electron microscopy images and helping with analysis. We are grateful to Mr. Vishwajeeth Pagala and the Center for Proteomics and Metabolomics core for protein identification and Mr. Ashutosh Mishra for help with statistical analysis of the protein dataset. Two OS PDX tumors were kindly provided by the Solid Tumor Network with the assistance of Dr. Asa Karlstrom, and FPKM reads obtained from RNA-seq analysis of two normal bone samples were a kind gift from Dr. Michael Dyer. We also wish to thank Dr. Shondra Miller and the Center for Advanced Genome Engineering (CAGE) for assisting with gRNA designs and Christian Melendez-Suchi for help with animal maintenance. The CAGE is funded in part by a grant from the National Cancer Institute P30 CA021765. We are grateful for support from Alex's Lemonade Stand Foundation 182026010 and the American Lebanese Syrian Associated Charities of St. Jude Children's Research Hospital. Lastly, we are appreciative of valuable comments on the manuscript provided by Drs. Kevin Freeman, Mark Hatley, and Charles Sherr.

AUTHOR CONTRIBUTIONS

Conceptualization, L.M.H. and R.K.W.; Data Curation, R.K.W.; Formal Analysis, R.K.W.; Funding Acquisition, L.M.H.; Investigation, R.K.W., A.R.F., M.J.M., and L.J.T.; Methodology, R.K.W.; Project administration, L.M.H. and R.K.W.; Resources, R.K.W.; Supervision, L.M.H.; Validation, R.W.K., A.R.F., and M.J.M.; Visualization, R.W.K.; Writing – Original Draft, R.K.W. and L.M.H.; Writing – Review & Editing – R.K.W. and L.M.H.

DECLARATION OF INTERESTS

The authors declare no competing interests.

Received: October 5, 2021
Revised: January 11, 2022
Accepted: March 15, 2022
Published: April 15, 2022

REFERENCES

Adamson, B., Norman, T.M., Jost, M., Cho, M.Y., Nuñez, J.K., Chen, Y., Villalta, J.E., Gilbert, L.A., Horlbeck, M.A., Hein, M.Y., et al. (2016). A multiplexed single-cell CRISPR screening platform enables systematic dissection of the unfolded protein response. Cell *167*, 1867–1882.e21. https://doi.org/10.1016/j.cell.2016.11.048.

Aparisi, T., Stark, A., and Ericsson, J.L. (1982). Human osteogenic sarcoma. Study of the ultrastructure, with special notes on the localization of alkaline and acid phosphatase. Int. Orthop. *6*, 171–179. https://doi.org/10.1007/bf00267727.

Behnke, J., and Hendershot, L.M. (2014). The large Hsp70 Grp170 binds to unfolded protein substrates in vivo with a regulation distinct from conventional Hsp70s. J. Biol. Chem. *289*, 2899–2907. https://doi.org/10.1074/jbc.M113.507491.

Chao, Y., Hu, K., Wang, X., and Wang, L. (2019). MicroRNA-552 promotes migration and invasion of osteosarcoma through targeting TIMP2. Biochem. Biophys. Res. Commun. *511*, 63–68. https://doi.org/10.1016/j.bbrc.2019.02.007.

Chen, X., Bahrami, A., Pappo, A., Easton, J., Dalton, J., Hedlund, E., Ellison, D., Shurtleff, S., Wu, G., Wei, L., et al. (2014). Recurrent somatic structural variations contribute to tumorigenesis in pediatric osteosarcoma. Cell Rep. *7*, 104–112. https://doi.org/10.1016/j.celrep.2014.03.003.

Cutrona, M.B., Beznoussenko, G.V., Fusella, A., Martella, O., Moral, P., and Mironov, A.A. (2013). Silencing of mammalian Sar1 isoforms reveals COPII-independent protein sorting and transport. Traffic *14*, 691–708. https://doi.org/10.1111/tra.12060.

Durfee, R.A., Mohammed, M., and Luu, H.H. (2016). Review of osteosarcoma and current management. Rheumatol. Ther. *3*, 221–243. https://doi.org/10.1007/s40744-016-0046-y.

Faustino-Rocha, A., Oliveira, P.A., Pinho-Oliveira, J., Teixeira-Guedes, C., Soares-Maia, R., Da Costa, R.G., Colaço, B., Pires, M.J., Colaço, J., Ferreira, R., et al. (2013). Estimation of rat mammary tumor volume using caliper and ultrasonography measurements. Lab. Anim. *42*, 217–224. https://doi.org/10.1038/laban.254.

Fox, R.M., Hanlon, C.D., and Andrew, D.J. (2010). The CrebA/Creb3-like transcription factors are major and direct regulators of secretory capacity. J. Cell Biol. *191*, 479–492. https://doi.org/10.1083/jcb.201004062.

Gelse, K., Pöschl, E., and Aigner, T. (2003). Collagens–structure, function, and biosynthesis. Adv. Drug Deliv. Rev. *55*, 1531–1546. https://doi.org/10.1016/j.addr.2003.08.002.

Gorur, A., Yuan, L., Kenny, S.J., Baba, S., Xu, K., and Schekman, R. (2017). COPII-coated membranes function as transport carriers of intracellular procollagen I. J. Cell Biol. *216*, 1745–1759. https://doi.org/10.1083/jcb.201702135.

Horiuchi, K., Tohmonda, T., and Morioka, H. (2016). The unfolded protein response in skeletal development and homeostasis. Cell Mol Life Sci. *73*, 2851–2869. https://doi.org/10.1007/s00018-016-2178-1.

Isakoff, M.S., Bielack, S.S., Meltzer, P., and Gorlick, R. (2015). Osteosarcoma: current treatment and a collaborative pathway to success. J. Clin. Oncol. *33*, 3029–3035. https://doi.org/10.1200/jco.2014.59.4895.

Ishikawa, T., Toyama, T., Nakamura, Y., Tamada, K., Shimizu, H., Ninagawa, S., Okada, T., Kamei, Y., Ishikawa-Fujiwara, T., Todo, T., et al. (2017). UPR transducer BBF2H7 allows export of type II collagen in a cargo- and developmental stage–specific manner. J. Cell Biol. *216*, 1761–1774. https://doi.org/10.1083/jcb.201609100.

Jian, Y.K., Zhu, H.Y., Wu, X.L., and Li, B. (2019). Thrombospondin 1 triggers osteosarcoma cell metastasis and tumor angiogenesis. Oncol. Res. *27*, 211–218. https://doi.org/10.3727/096504018x15208993118389.

Kansara, M., Teng, M.W., Smyth, M.J., and Thomas, D.M. (2014). Translational biology of osteosarcoma. Nat. Rev. Cancer *14*, 722–735. https://doi.org/10.1038/nrc3838.

Konermann, S., Brigham, M.D., Trevino, A.E., Joung, J., Abudayyeh, O.O., Barcena, C., Hsu, P.D., Habib, N., Gootenberg, J.S., Nishimasu, H., et al. (2015). Genome-scale transcriptional activation by an engineered CRISPR-Cas9 complex. Nature *517*, 583–588. https://doi.org/10.1038/nature14136.

Lorenz, S., Barøy, T., Sun, J., Nome, T., Vodák, D., Bryne, J.C., Håkelien, A.M., Fernandez-Cuesta, L., Möhlendick, B., Rieder, H., et al. (2016). Unscrambling the genomic chaos of osteosarcoma reveals extensive transcript fusion, recurrent rearrangements and frequent novel TP53 aberrations. Oncotarget *7*, 5273–5288. https://doi.org/10.18632/oncotarget.6567.

Luu, H.H., Kang, Q., Park, J.K., Si, W., Luo, Q., Jiang, W., Yin, H., Montag, A.G., Simon, M.A., Peabody, T.D., et al. (2005). An orthotopic model of human osteosarcoma growth and spontaneous pulmonary metastasis. Clin. Exp. Metastasis *22*, 319–329. https://doi.org/10.1007/s10585-005-0365-9.

Ma, W., and Goldberg, J. (2016). TANGO1/cTAGE5 receptor as a polyvalent template for assembly of large COPII coats. Proc. Natl. Acad. Sci. U S A *113*, 10061–10066. https://doi.org/10.1073/pnas.1605916113.

Ma, Y., Brewer, J.W., Diehl, J.A., and Hendershot, L.M. (2002). Two distinct stress signaling pathways converge upon the CHOP promoter during the mammalian unfolded protein response. J. Mol. Biol. *318*, 1351–1365. https://doi.org/10.1016/s0022-2836(02)00234-6.

Maiers, J.L., Kostallari, E., Mushref, M., Deassuncao, T.M., Li, H., Jalan-Sakrikar, N., Huebert, R.C., Cao, S., Malhi, H., and Shah, V.H. (2017). The unfolded protein response mediates fibrogenesis and collagen I secretion through regulating TANGO1 in mice. Hepatology *65*, 983–998. https://doi.org/10.1002/hep.28921.

Martin, J.W., Squire, J.A., and Zielenska, M. (2012). The genetics of osteosarcoma. Sarcoma *2012*, 627254. https://doi.org/10.1155/2012/627254.

Mathivanan, S., Fahner, C.J., Reid, G.E., and Simpson, R.J. (2012). ExoCarta 2012: database of exosomal proteins, RNA and lipids. Nucleic Acids Res. *40*, D1241–D1244. https://doi.org/10.1093/nar/gkr828.

Mccaughey, J., Stevenson, N.L., Cross, S., and Stephens, D.J. (2019). ER-to-Golgi trafficking of procollagen in the absence of large carriers. J. Cell Biol. *218*, 929–948. https://doi.org/10.1083/jcb.201806035.

Meazza, C., and Scanagatta, P. (2016). Metastatic osteosarcoma: a challenging multidisciplinary treatment. Expert Rev. Anticancer Ther. *16*, 543–556. https://doi.org/10.1586/14737140.2016.1168697.

Mellor, P., Deibert, L., Calvert, B., Bonham, K., Carlsen, S.A., and Anderson, D.H. (2013). CREB3L1 is a metastasis suppressor that represses expression of genes regulating metastasis, invasion, and angiogenesis. Mol. Cell. Biol. *33*, 4985–4995. https://doi.org/10.1128/MCB.00959-13.

Misaghi, A., Goldin, A., Awad, M., and Kulidjian, A.A. (2018). Osteosarcoma: a comprehensive review. SICOT-J *4*, 12. https://doi.org/10.1051/sicotj/2017028.

Moriarity, B.S., Otto, G.M., Rahrmann, E.P., Rathe, S.K., Wolf, N.K., Weg, M.T., Manlove, L.A., Larue, R.S., Temiz, N.A., Molyneux, S.D., et al. (2015). A Sleeping Beauty forward genetic screen identifies new genes and pathways driving osteosarcoma development and metastasis. Nat. Genet. *47*, 615–624. https://doi.org/10.1038/ng.3293.

Murakami, T., Saito, A., Hino, S., Kondo, S., Kanemoto, S., Chihara, K., Sekiya, H., Tsumagari, K., Ochiai, K., Yoshinaga, K., et al. (2009).

Signalling mediated by the endoplasmic reticulum stress transducer OASIS is involved in bone formation. Nat. Cell Biol. *11*, 1205–1211. https://doi.org/10.1038/ncb1963.

Mutsaers, A.J., and Walkley, C.R. (2014). Cells of origin in osteosarcoma: mesenchymal stem cells or osteoblast committed cells? Bone *62*, 56–63. https://doi.org/10.1016/j.bone.2014.02.003.

Oakes, S.A. (2020). Endoplasmic reticulum stress signaling in cancer cells. Am. J. Pathol. *190*, 934–946. https://doi.org/10.1016/j.ajpath.2020.01.010.

Raote, I., and Malhotra, V. (2021). Tunnels for protein export from the endoplasmic reticulum. Annu. Rev. Biochem. *90*, 605–630. https://doi.org/10.1146/annurev-biochem-080120-022017.

Raote, I., Ortega-Bellido, M., Santos, A.J., Foresti, O., Zhang, C., Garcia-Parajo, M.F., Campelo, F., and Malhotra, V. (2018). TANGO1 builds a machine for collagen export by recruiting and spatially organizing COPII, tethers and membranes. Elife *7*, e32723. https://doi.org/10.7554/eLife.32723.

Richards, C.I., Srinivasan, R., Xiao, C., Mackey, E.D.W., Miwa, J.M., and Lester, H.A. (2011). Trafficking of α4* nicotinic receptors revealed by superecliptic phluorin: effects OF a β4 amyotrophic lateral sclerosis-associated mutation and chronic exposure to nicotine. J. Biol. Chem. *286*, 31241–31249. https://doi.org/10.1074/jbc.M111.256024.

Rickel, K., Fang, F., and Tao, J. (2017). Molecular genetics of osteosarcoma. Bone *102*, 69–79. https://doi.org/10.1016/j.bone.2016.10.017.

Rose, M., Schubert, C., Dierichs, L., Gaisa, N.T., Heer, M., Heidenreich, A., Knüchel, R., and Dahl, E. (2014). OASIS/CREB3L1 is epigenetically silenced in human bladder cancer facilitating tumor cell spreading and migration in vitro. Epigenetics *9*, 1626–1640. https://doi.org/10.4161/15592294.2014.988052.

Rusch, M., Nakitandwe, J., Shurtleff, S., Newman, S., Zhang, Z., Edmonson, M.N., Parker, M., Jiao, Y., Ma, X., Liu, Y., et al. (2018). Clinical cancer genomic profiling by three-platform sequencing of whole genome, whole exome and transcriptome. Nat. Commun. *9*, 3962. https://doi.org/10.1038/s41467-018-06485-7.

Rusk, A., Mckeegan, E., Haviv, F., Majest, S., Henkin, J., and Khanna, C. (2006). Preclinical evaluation of antiangiogenic thrombospondin-1 peptide mimetics, ABT-526 and ABT-510, in companion dogs with naturally occurring cancers. Clin. Cancer Res. *12*, 7444–7455. https://doi.org/10.1158/1078-0432.Ccr-06-0109.

Saito, K., Chen, M., Bard, F., Chen, S., Zhou, H., Woodley, D., Polischuk, R., Schekman, R., and Malhotra, V. (2009). TANGO1 facilitates cargo loading at endoplasmic reticulum exit sites. Cell *136*, 891–902. https://doi.org/10.1016/j.cell.2008.12.025.

Sampieri, L., Di Giusto, P., and Alvarez, C. (2019). CREB3 transcription factors: ER-Golgi stress transducers as hubs for cellular homeostasis. Front. Cell Dev. Biol. *7*, 123. https://doi.org/10.3389/fcell.2019.00123.

Sarmah, S., Barrallo-Gimeno, A., Melville, D.B., Topczewski, J., Solnica-Krezel, L., and Knapik, E.W. (2010). Sec24D-dependent transport of extracellular matrix proteins is required for zebrafish skeletal morphogenesis. PLoS One *5*, e10367. https://doi.org/10.1371/journal.pone.0010367.

Schneider, C.A., Rasband, W.S., and Eliceiri, K.W. (2012). NIH Image to ImageJ: 25 years of image analysis. Nat. Methods *9*, 671–675. https://doi.org/10.1038/nmeth.2089.

Steiner, G.C., Forest, M., and Vacher-Lavenu, M.C. (2006). Ultrastructure of low-grade intraosseous osteosarcoma of bone: a comparative study with fibrous dysplasia and parosteal osteosarcoma. Ultrastruct. Pathol. *30*, 293–299. https://doi.org/10.1080/019131290969479.

Stewart, E., Federico, S.M., Chen, X., Shelat, A.A., Bradley, C., Gordon, B., Karlstrom, A., Twarog, N.R., Clay, M.R., Bahrami, A., et al. (2017). Orthotopic patient-derived xenografts of paediatric solid tumours. Nature *549*, 96–100. https://doi.org/10.1038/nature23647.

Talbot, L.J., Chabot, A., Funk, A., Nguyen, P., Wagner, J., Ross, A., Tillman, H., Davidoff, A., Gottschalk, S., and Derenzo, C. (2021). A novel orthotopic implantation technique for osteosarcoma produces spontaneous metastases and illustrates dose-dependent efficacy of B7-H3-CAR T cells. Front. Immunol. *12*, 691741. https://doi.org/10.3389/fimmu.2021.691741.

Tanenbaum, M.E., Gilbert, L.A., Qi, L.S., Weissman, J.S., and Vale, R.D. (2014). A protein-tagging system for signal amplification in gene expression and fluorescence imaging. Cell *159*, 635–646. https://doi.org/10.1016/j.cell.2014.09.039.

Van Krieken, R., Tsai, Y.L., Carlos, A.J., Ha, D.P., and Lee, A.S. (2021). ER residential chaperone GRP78 unconventionally relocalizes to the cell surface via endosomal transport. Cell Mol Life Sci. *78*, 5179–5195. https://doi.org/10.1007/s00018-021-03849-z.

Volpert, O.V., Stellmach, V., and Bouck, N. (1995). The modulation of thrombospondin and other naturally occurring inhibitors of angiogenesis during tumor progression. Breast Cancer Res. Treat. *36*, 119–126. https://doi.org/10.1007/BF00666034.

Ward, A.K., Mellor, P., Smith, S.E., Kendall, S., Just, N.A., Vizeacoumar, F.S., Sarker, S., Phillips, Z., Alvi, R., Saxena, A., et al. (2016). Epigenetic silencing of CREB3L1 by DNA methylation is associated with high-grade metastatic breast cancers with poor prognosis and is prevalent in triple negative breast cancers. Breast Cancer Res. *18*, 12. https://doi.org/10.1186/s13058-016-0672-x.

Weekes, D., Kashima, T.G., Zandueta, C., Perurena, N., Thomas, D.P., Sunters, A., Vuillier, C., Bozec, A., El-Emir, E., Miletich, I., et al. (2016). Regulation of osteosarcoma cell lung metastasis by the c-Fos/AP-1 target FGFR1. Oncogene *35*, 2852–2861. https://doi.org/10.1038/onc.2015.344.

Williams, A.H., Schwinn, C.P., and Parker, J.W. (1976). The ultrastructure of osteosarcoma. A review of twenty cases. Cancer *37*, 1293–1301. https://doi.org/10.1002/1097-0142.

Yoshida, H., Matsui, T., Yamamoto, A., Okada, T., and Mori, K. (2001). XBP1 mRNA is induced by ATF6 and spliced by IRE1 in response to ER stress to produce a highly active transcription factor. Cell *107*, 881–891. https://doi.org/10.1016/s0092-8674(01)00611-0.

Yuan, J., Ossendorf, C., Szatkowski, J.P., Bronk, J.T., Maran, A., Yaszemski, M., Bolander, M.E., Sarkar, G., and Fuchs, B. (2009). Osteoblastic and osteolytic human osteosarcomas can be studied with a new xenograft mouse model producing spontaneous metastases. Cancer Invest. *27*, 435–442. https://doi.org/10.1080/07357900802491477.

Yuan, L., Kenny, S.J., Hemmati, J., Xu, K., and Schekman, R. (2018). TANGO1 and SEC12 are copackaged with procollagen I to facilitate the generation of large COPII carriers. Proc. Natl. Acad. Sci. U S A *115*. E12255–e12264. https://doi.org/10.1073/pnas.1814810115.

Zhang, H., Zhang, J., Meng, F., Zhu, H., Yan, H., Guo, Y., and Zhang, S. (2019). MicroRNA-93 promotes the tumorigenesis of osteosarcoma by targeting TIMP2. Biosci. Rep. *39*. BSR20191237. https://doi.org/10.1042/bsr20191237.

Zhang, L., and Yu, D. (2019). Exosomes in cancer development, metastasis, and immunity. Biochim. Biophys. Acta Rev. Cancer *1871*, 455–468. https://doi.org/10.1016/j.bbcan.2019.04.004.

Zhang, X.B., Zhang, R.H., Su, X., Qi, J., Hu, Y.C., Shi, J.T., Zhang, K., Wang, K.P., and Zhou, H.Y. (2021). Exosomes in osteosarcoma research and preclinical practice. Am. J. Transl. Res. *13*, 882–897.

Zhou, J.Y., Afjehi-Sadat, L., Asress, S., Duong, D.M., Cudkowicz, M., Glass, J.D., and Peng, J. (2010). Galectin-3 is a candidate biomarker for amyotrophic lateral sclerosis: discovery by a proteomics approach. J. Proteome Res. *9*, 5133–5141. https://doi.org/10.1021/pr100409r.

Zhou, X., Edmonson, M.N., Wilkinson, M.R., Patel, A., Wu, G., Liu, Y., Li, Y., Zhang, Z., Rusch, M.C., Parker, M., et al. (2016). Exploring genomic alteration in pediatric cancer using ProteinPaint. Nat. Genet. *48*, 4–6. https://doi.org/10.1038/ng.3466.

STAR★METHODS

KEY RESOURCES TABLE

REAGENT or RESOURCE	SOURCE	IDENTIFIER
Antibodies		
mouse anti-procollagen I	Abcam	ab90395
rabbit anti-Collagen I	Abcam	ab34710
rabbit anti-GRP170	Behnke and Hendershot (2014)	N/A
rabbit anti-human BiP	Dr. Ineke Braakman, Utrecht University, Netherlands	N/A
rabbit anti-CHOP	Ma et al. (2002)	N/A
mouse anti-SAR1A	Santa Cruz	sc-130463
rabbit anti-SEC24D	Cell Signaling	14687s
mouse anti-GAPDH	Millipore	MAB374
mouse anti-SP1.D8	DSHB by Dr. H Furthmayr	SP1.D8
mouse anti-M-38	DSHB by Dr. J.A. McDonald	M-38
rabbit anti-TIMP1	Cell Signaling	8946S
rabbit anti-Vimentin	Abcam	ab137321
IRDye 800CW goat anti- mouse IgG	LiCor Biosciences	925-32210
IRDye 680RD goat anti- mouse IgG	LiCor Biosciences	925-68070
IRDye 800CW goat anti- rabbit	LiCor Biosciences	925-32211
IRDye 680RD goat anti- rabbit	LiCor Biosciences	925-68071
Goat Anti-Mouse IgG(H + L), Multi-Species SP ads-HRP	SouthernBiotech	1038-05
Goat Anti-Rabbit IgG(H + L), Mouse/Rat/ Human ads-HRP	SouthernBiotech	4049-05
Goat Anti-Rabbit IgG-Alexa Fluor® 488	SouthernBiotech	4030-30
Goat Anti-Mouse Ig, Human ads-Alexa Fluor® 555	SouthernBiotech	1010-32
Biological samples		
OS patient derived xenografts	Childhood Solid Tumor Network	https://www.stjude.org/research/why-st-jude/data-tools/childhood-solid-tumor-network.html
Chemicals, peptides, and recombinant proteins		
5-bromo-2'-deoxyuridine	Sigma-Aldrich	B5002
L-glutamine	Corning	25-005-CI
SuperScript™ III Reverse Transcriptase	Invitrogen	18080-044
AmpliTaq™ DNA Polymerase	Applied BioSystems	N8080161
Agarose	Sigma-Aldrich	11 685 678 001
SYBR® Green	Applied Biosystems	4367659
GeneCellin HTC	BulldogBio	HTC0750
Express [^{35}S] Labeling Mix	Perkin Elmer	NEG072-007
DMEM labeling media without Met/Cys	Corning	17-204-CI
PBS	Corning	21-031-CV
Tris-HCl	RPI	77-86-1
NP-40	Sigma-Aldrich	74385

(*Continued on next page*)

Continued

REAGENT or RESOURCE	SOURCE	IDENTIFIER
Sodium deoxycholate	Sigma-Aldrich	D6750
NaCl	Fisher Scientific	S271-10
PMSF	Sigma-Aldrich	P7626
Protease inhibitor cocktail	Roche	5056489001
Protein A agarose	Repligen	CA-PRI-0100
Gelatin from cold water fish skin	Sigma-Aldrich	G7041-100G
Tween20	Thermo Fisher	BP337-100
ECL Western Blotting Substrate	Pierce	32106
Puromycin	InVivoGen	ant-pr-1
G418 geneticin	InVivoGen	ant-gn-1
Triton X-100	Sigma-Aldrich	X100
Bovine Serum Albumin	Sigma-Aldrich	A4503
ProLong™ Gold Antifade Mountant with DAPI	ThermoFisher	P36935
IVISbrite D-Luciferin Potassium Salt Bioluminescent Substrate (1 g) (XenoLight)	PerkinElmer	122799
Trichloroacetic acid	Thermo Fisher	A322-500
2-β mercaptoethanol	Sigma-Aldrich	M6250
GelCode-Blue	Thermo Scientific	24590
Dithiothreitol	Sigma-Aldrich	D0632
Iodoacetamide	Sigma-Aldrich	I-4386
Paraformaldehyde	Electron Microscopy Sciences	15713
Critical commercial assays		
RNeasy Plus Kit	Qiagen	74134
High Capacity cDNA Reverse Transcription Kit	Applied Biosystems	4368814
Quant-iT RiboGreen assay	Life Technologies	R32700
High Sensitivity RNA ScreenTape assay	Agilent	5067-5579; 5067-5580
LabChip RNA Pico Sensitivity assay	Perkin Elmer	CLS960012
TruSeq Stranded Total RNA Library Prep Kit	Illumina	20020599
Caliper LabChip GX DNA High Sensitivity Reagent Kit	Perkin Elmer	CLS760672
D1000 ScreenTape assay	Agilent	5067-5582; 5067-5583
Quant-iT PicoGreen ds DNA assay	Life Technologies	P7589
In-Fusion HD cloning kit	Takara	638917
Non-Radioactive Cell Proliferation Assay (MTS)	Promega	G5421
Cell Invasion Assay	Cell Biolabs	CBA-110-COL
Deposited data		
Pediatric Cancer Data Portal: Clinical Genomics dataset	Rusch et al., 2018	https://pecan.stjude.cloud/
RNA sequencing data	This paper	GEO: GSE197158
Proteomics data	This paper	ProteomeXchange: PXD031620
Experimental models: Cell lines		
hFOB1.19	ATCC	CRL-11372
SaOS2	Dr. Michael A. Dyer	N/A
U2OS	Dr. Michael A. Dyer	N/A
143B	Dr. Michael A. Dyer	N/A

(*Continued on next page*)

Continued

REAGENT or RESOURCE	SOURCE	IDENTIFIER
293T	ATCC	CRL-3216
Experimental models: Organisms/strains		
Homozygous CD1-Nude female mice	Charles River	Crl:CD1-*Foxn1*^{nu}
Oligonucleotides		
See Table S3 for Reverse Transcription & qRT-PCR Primer Pairs	This paper	(Yoshida et al., 2001)
See Table S4 for sgRNAs Tested	This paper	(Konermann et al., 2015)
Recombinant DNA		
See Table S2 for Plasmid constructs	This paper	(Adamson et al., 2016; Richards et al., 2011; Tanenbaum et al., 2014)
Software and algorithms		
ImageJ	Schneider et al. (2012)	https://imagej.nih.gov/ij/
Image Studio™	LI-COR®	https://www.licor.com/bio/image-studio/
Prism 9	GraphPad Software	www.graphpad.com
Other		
PVDF membranes	Millipore	IPFL00010
Film	Denville Scientific	E3018
Precast 4%–15% gradient gel	Bio-Rad	4568086

RESOURCE AVAILABILITY

Lead contact

Further information and requests for resources and reagents should be directed to and will be fulfilled by the lead contact, Linda M. Hendershot (Linda.hendershot@stjude.org).

Materials availability

All plasmids in this study originally were purchased from Addgene and modified as described. Cell lines and plasmids generated within this study are available upon request.

Data and code availability

- RNA sequencing data have been deposited at Gene Expression Omnibus and the mass spectrometry data have been deposited to the ProteomeXchange Consortium via the PRIDE partner. The datasets are publicly available as of the date of publication and accession numbers are listed in the key resources table.
- This paper does not report original code.
- Any additional information required to reanalyze the data reported in this paper is available from the lead contact upon request.

EXPERIMENTAL MODEL AND SUBJECT DETAILS

Cells

The hFOB1.19 cells (ATCC) were cultured at 34 °C with 5% CO2 and grown in DMEM/F-12, no phenol red (Gibco), supplemented with 10% fetal bovine serum and 1% L-glutamine. Osteosarcoma cell lines SaOS2, U2OS, and 143B were gifts from Dr. Michael A. Dyer (St. Jude Children's Research Hospital), cultured at 37 °C with 5% CO2 in Dulbecco's modified Eagle medium (Corning™), supplemented with 10% fetal bovine serum and 1% L-glutamine. 143B is additionally cultured in 0.015 mg/mL 5-bromo-2′-deoxyuridine (Sigma-Aldrich), per guidelines of ATCC.

Lentiviral transduction was used to create stable transgenic cell lines. Lentiviruses were produced by calcium phosphate transfection of HEK293T cells with standard third generation packaging plasmids combined with the specific transfer plasmids. Culture supernatants containing virus were harvested ~48 h post-transfection and passed through a 0.45uM PVDF filter (Millipore). To introduce the SunTag system, SaOS2 and 143B cells were first stably transduced with pHRdSV40-dCas9-10xGCN4_v4-P2A-BFP (Addgene plasmid #60903) and pHRdSV40-scFv-GCN4-sfGFP-VP64-GB1-NLS (Addgene plasmid #60904). After ~1–2 weeks, bulk cultures were sorted for cells expressing both BFP and GFP using a BD FACSAria III cell sorter (BD Biosciences). The SunTag system-integrated lines are hereby referred to as SaOS2.ST and 143B.ST. To restore SAR1A and SEC24D in SaOS2.ST cells, they were stably transduced with pBA439.bU6.SEC24D.g2_mU6.SAR1A.g28 virus. 48 h post-transduction cells were placed in a 2 ug/mL puromycin selection (InvivoGen) for a minimum of five days to select for SaOS2.ST(+COPII) cells. 143B(+COPII) cells were generated via the same method of stable transduction of virus and selection, the only difference is SAR1A.g64 was used in place of SAR1A.g28. Similarly, to introduce collagen synthesis, 143B.ST cells were stably transduced with pBA439.bU6.COL1A1.g1_mU6.COL1A2.g35 virus, and 48 h post-transduction were placed in a 1ug/mL G418 geneticin (InvivoGen) for a minimum of five days to select for 143B.ST(+COL1) cells. Both the sgRNA expression cell lines were stably transduced with pHIV- Luc-YFP viral media and sorted for BFP/GFP/mCherry/YFP expressing populations. Additionally, the parental non-sgRNA expressing lines, SaOS2.ST and 143B.ST were also stably transduced with pHIV-Luc-YFP virus and bulk-sorted for a BFP/GFP/YFP(+) population. A summary of each construct and gRNA sequences can be found in Tables S2 and S4 respectively.

Cell Lines	Final Cell Sort Populations	Contains
SaOS2.ST	BFP, GFP,YFP	dCas9, VP64, luciferase
SaOS2.ST(+COPII)	BFP,GFP,mCherry,YFP	dCas9, VP64, COPII-gRNAs, luciferase
143B.ST	BFP, GFP,YFP	dCas9, VP64, luciferase
143B.ST(+COL1)	BFP,GFP,mCherry,YFP	dCas9, VP64, COL1-gRNAs, luciferase
143B.ST(+COPII)	BFP,GFP,mCherry,YFP	dCas9, VP64, COPII-gRNAs, luciferase

Animals

Homozygous CD1-Nude female mice (Crl:CD1-*Foxn1*^{nu}) purchased from Charles River were housed and cared for in accordance with both the Animal Use and Care Committee and the Animal Research Center at St. Jude Children's Research Hospital, adhering to the National Institutes of Health guidelines. Animals were housed 5 per cage and at 9 weeks of age 1 × 10^5 143B.ST or 143B.ST(+COPII) cells were implanted into the right proximal anterior tibia of mice, n = 10 per cell line using an orthotopic implantation method developed by one of the authors (Talbot et al., 2021). The mice post-operatively recovered on a heating pad for five days receiving buprenorphine 0.03 mg/mL (Patterson Veterinary, Greeley, CO), subcutaneously at 0.1 mg/kg and amoxicillin 400 mg/50 mls (Sandoz, Princeton, NJ) was added to a 350 mL water bottle at a dosage of 50 mg/kg for one week. Outcome measurements began three days post-surgery. Tumor implantation was assessed, and growth was monitored weekly by bioluminescent imaging until tumor volume reached 20% body mass or the animal became moribund. Briefly, five to 10 min prior to imaging, animals were injected intraperitoneally with D-Luciferin (15 mg/mL in sterile saline) at a dose of 150 mg/kg (10 μL/g of body weight). After administration, animals were anesthetized using Isoflurane (1.5%–2% delivered in 100% O_2 at 1 L/min) administered through a nosecone. Following imaging, animals recovered under observation. In addition to bioluminescent imaging, caliper measurements of the width and length of palpable tumors were recorded weekly the same day as imaging. Tumor volume was calculated according to the formula V = (W2 × L)/2 (Faustino-Rocha et al., 2013).

METHOD DETAILS

mRNA expression studies

For all mRNA-based assays, total RNA was isolated from cell lines using the RNeasy Kit (Qiagen). To detect XBP-1 splicing, isolated RNA was reverse transcribed using SuperScript™ III Reverse Transcriptase (Invitrogen) per manufacturer's protocol. PCR amplification was performed using 0.5-1ug of cDNA with AmpliTaq™ DNA Polymerase in Buffer II (Applied Biosystems) and 10uM of primer pairs for either XBP1.Uand S or GAPDH (listed in Table S3). PCR-amplified products were separated on 2% agarose (Sigma-Aldrich) gels in TBE buffer and visualized by staining with ethidium bromide. Analysis of other

transcripts was performed using real-time PCR. Isolated RNA was reverse transcribed using the High Capacity cDNA Reverse Transcription Kit (Applied Biosystems) and subjected to SYBR® Green chemistry-based qPCR according to the manufacturer's protocol using the QuantStudio 3 Real-time PCR System (Applied Biosystems). Primer pairs were obtained from (ThermoFisher Scientific) and sequences are listed in Table S3.

RNA-seq analysis was performed on the hFOB1.19 osteoblast line as a control, and on the SaOS2, 143B, and U2OS osteosarcoma lines and two OS-PDXs by the Genome Sequencing Facility at St. Jude Children's Research Hospital. Briefly, isolated RNA was quantified using the Quant-iT RiboGreen assay (Life Technologies) and quality checked by 2100 Bioanalyzer RNA 6000 Nano assay (Agilent) 4200 TapeStation High Sensitivity RNA ScreenTape assay (Agilent) or LabChip RNA Pico Sensitivity assay (PerkinElmer) prior to library generation. Libraries were prepared from total RNA with the TruSeq Stranded Total RNA Library Prep Kit according to the manufacturer's instructions (Illumina, PN, 20020599).

Metabolic labeling experiments

To analyze the effects of restored SAR1A and SEC24D on collagen-I secretion in SaOS2 cells, transient expression experiments were used first. SaOS2 cells were seeded 24 h prior to transfection, which was performed using GeneCellin HTC (Bulldog Bio) according to the manufacturer's protocol. Control cells were mock transfected, and test cells were transfected with 1 ug of pDEST47-SAR1A (Addgene), alone, 1ug of pmCherry-SEC24D (Addgene) alone, or 1 ug of each together. 24 h post-transfection, cells were analyzed. Alternatively, stable SaOS.ST and SaOS.ST(+COPII) cells were used. In experiments to confirm that a combination of reduced COPII components and collagen expression were responsible for the abnormal ER phenotype associated with OS, 143B.ST and 143B.ST(+COL) were compared. In each case, cell lines were labeled for 16 h with 0.1 mCi of Express [^{35}S] Labeling Mix (PerkinElmer) in DMEM labeling media without Met/Cys (Corning) that was supplemented with 1% L-glutamine and 1% fetal bovine serum previously dialyzed against PBS. To identify secreted collagen, culture supernatants were harvested and centrifuged at 500 rcf for 5 min in a refrigerated Eppendorf centrifuge to pellet any detached cells. To analyze lysates, cells were washed twice with PBS and lysed in 1 mL NP-40 lysis buffer (50mM Tris-HCl pH 7.5, 150 mM NaCl, 0.5%sodium deoxycholate, and 0.5% NP-40, supplemented with 0.1 mM PMSF and a protease inhibitor cocktail) on ice for 20 min. Lysates were clarified by centrifugation at 21,000 rcf for 15 min. Collagen was isolated from cell lysates and culture supernatants with the immune reagents indicated in the figure legends. Note: Due to the discontinued production of anti-[COL-1] #ab90395 during the course of this study, later experiments were done with anti-Collagen I #ab34710s. In all cases, 0.5 ug of antibody was added to the clarified samples and incubated at 4 °C overnight while rotating. Protein A agarose was added for 1 h the following morning. Immunoprecipitated complexes were washed 3 times with NP-40 washing buffer (50mM Tris-HCl pH 7.5, 400 mM NaCl, 0.5% DOC. and 0.5% NP-40) and analyzed by reducing SDS-PAGE. A Hyphoon FLA 9500 phosphorimager (GE Healthcare, Pittsburgh, PA) was used to detect signals, viewed using ImageQuant TL software (GE Healthcare, Pittsburgh, PA).

Immunoblotting

Clarified cell lysates were electrophoresed under reducing conditions on SDS-polyacrylamide gels and transferred to PVDF membranes (Millipore #IPFL00010). Membranes were blocked with either 5% non-fat milk or fish gelatin (Sigma #G7041-100G) based on antibody manufacturer recommendations for 30 min at room temperature and incubated overnight in primary antibodies on an orbital rocker at 4C. Membranes were serially washed in TBS and TBST (0.1%Tween 20) and incubated in secondary reagents for 1 h at room temperature on an orbital rocker. Finally, membranes were serially washed again and imaged on a Li-Cor and visualized using Image Studio™ (LI-COR Biosciences, Inc., Lincoln, NE). Primary antibodies used were rabbit anti-GRP170 (Behnke and Hendershot, 2014), rabbit anti-human BiP, kindly provided by Ineke Braakman (Utrecht University, Utrecht, Netherlands), rabbit anti-CHOP (Ma et al., 2002), mouse anti-HSC70 (Santa Cruz), mouse anti-SAR1A (Santa Cruz), rabbit anti-SEC24D (Cell Signaling), mouse anti-GAPDH (Millipore), rabbit anti-TIMP1 (Cell Signaling), and rabbit anti-vimentin (Abcam). The SP1.D8 monoclonal antibody was deposited to the DSHB by Dr. H Furthmayr (DSHB Hybridoma Product SP1.D8), and M−38 was deposited by Dr. J.A. McDonald (DSHB Hybridoma Product M−38). Species-specific secondary reagents for developing immunoblots on the Licor were purchased from LiCor Biosciences. Westerns developed on film (Denville Scientific #E3018) used HRP

conjugated secondary antibodies purchased from SouthernBiotech and ECL Western Blotting Substrate (Pierce).

Transmission electron microscopy

For ultrastructural analysis, cells were seeded on tissue culture dishes. Upon reaching a confluency of ~70% samples were fixed as monolayers in 0.1M cacodylate buffer containing 2.5% glutaraldehyde and 2% paraformaldehyde, then scraped and pelleted for further processing by the Cell and Tissue Imaging core. Samples were post-fixed in osmium tetroxide and contrasted with uranyl acetate. Dehydration was performed by incubating in increasing concentrations of ethanol to 100% followed by 100% propylene oxide. Samples were infiltrated with EmBed-812 and polymerized at 80°C, after which they were sectioned at ~70 nm on a Leica (Wetzlar, Germany) ultramicrotome, mounted on bare copper support grids, and examined in a ThermoFisher Scientific (Hillsboro, OR) TF20 transmission electron microscope. Images were captured on an Advanced Microscopy Techniques camera system (Woburn, MA). Unless otherwise stated, all reagents were sourced from Electron Microscopy Sciences (Hatfield, PA).

CRISPRa cloning using the SunTag system

Plasmid constructs are listed in Table S2. The perturb-seq multiple gRNA expression vector backbone, pBA439 (Addgene plasmid #85967), was modified by restriction enzyme digestion at NheI and EcoRI sites to remove the puromycin-T2A-TagBFP fragment. In-Fusion HD cloning (Takara) was used to insert a puromycin-T2A-mCherry amplified fragment into the cut vector thereby generating the pBA439_puro.mCherry backbone. Alternatively, the NheI/EcoRI digested pBA439 backbone was used in combination with Gibson Assembly to insert a fragment containing the neomycin resistance gene and a T2A-mCherry gene thus generating pBA439_Neo.mCherry backbone.

The two single-guide expression vectors (pMJ114, Addgene plasmid #85995 and pMJ179, Addgene plasmid #85996) were double RE digested with BlpI /BstxI in NEB buffer 2.1 for 30 min at 37ºC. The buffer composition was then adjusted to final concentration of 100mM NaCl and 50mM Tris and incubated for another 30 min at 37ºC before inactivation at 80ºC for 20 min. The reactions were dephosphorylated with rAPid Alkaline Phosphatase (Roche, No. 04 898 133 001) and purified using Wizard® SV Gel and PCR Clean-Up System (Promega A9281). Forward and reverse gRNAs listed in Table S4 included BlpI /BstxI overhangs and were annealed using 100uM oligos at a 1:1 ratio in T4 ligation buffer (NEB B0202S) and T4 PNK (NEB M0201S). Incubated in a thermocycler at 37ºC for 30 min, 95ºC for 5 min and decreased 5ºC/min to 25ºC. Annealed gRNAs were diluted 1:200 in nuclease free water and inserted into the single-guide digested backbones in a Quick Ligation reaction (NEB M2200S) using 50 ng of vector to 1 ul of 1:200 annealed gRNA and incubated at 25ºC for 10 min before transformation of NEB stable cells (NEB C3040).

Successful sgRNA expression plasmids were PCR amplified at regions flanking the sgRNA expression cassettes from oligos designed with overhangs to facilitated Gibson assembly into the multi-guide pBA439_ backbone. Phusion polymerase (Thermo Scientific #F-530S) reactions were incubated in a thermocycler at 98ºC for 30 s followed by 30 cycles of 98ºC for 10 s, 58ºC for 20 s and 72ºC for 15 s, followed by a final extension of 72ºC for 5 min. PCR Products were either used immediately for Gibson assembly or purified and stored at −20ºC. For dual gRNA expression cassette assembly, the pBA439_backbones were double RE digested with XhoI/HpaI in Cutsmart Buffer (NEB) at 37ºC, for 60 min and agarose gel purified. The Gibson assembly reactions used 2-fold excess of the PCR amplified gRNA cassettes relative to the pBA439_backbone in a 5ul total reaction of NEBuilder HiFi DNA Assembly Master Mix (NEB E2621S). Reactions were incubated in a thermocycler at 50 °C for 60 min before transformation into NEB stable cells. A combination of *SAR1A* and *SEC24D* gene-targeting sgRNA cassettes were assembled into pBA439_backbone, which contained puromycin resistance and mCherry genes (pBA439_puro.mCherry) and *COL1A1* and *COL1A2* targeting gRNA cassettes were Gibson-assembled into the pBA439 backbone containing neomycin resistance and mCherry genes (pBA439_Neo.mCherry). All gRNA sequences are listed in Table S4.

Lastly, pHIV-Luc-ZsGreen (Addgene plasmid #39196) was modified by digestion at ClaI/BstXI sites to remove ZsGreen. A PCR-amplified YFP fragment was inserted using In-Fusion HD (Takara) in place of ZsGreen generating a pHIV-Luc-YFP plasmid.

Microscopy

hFOB1.19 and SaOS2 cells were grown on 35 mm glass bottom Matek dishes to 50% confluency. 24hrs after plating dishes were washed twice with PBS and fixed with 4% Paraformaldehyde for 20 min at room temperature and then rinsed again with PBS. Cells were permeabilized with 0.3% TX-100 in PBS for 10 min, followed by a PBS rinse and blocking (5% BSA and 0.1% TX-100 in PBS) for 1 h. Cells were incubated with both mouse anti-Sp1.d8 and rabbit anti-GRP170 in antibody dilution buffer of (1% BSA and 0.1% TX-100 in PBS) for 1 h at room temperature followed by a rinse in fresh antibody dilution buffer on an orbital rocker for 5 min. Cells were then incubated in antibody dilution buffer containing both fluorochrome-conjugated anti-mouse Ig and anti-rabbit Ig antibodies for 45 min at 37 °C in a humidified chamber. After rinsing three times, coverslips were mounted with ProLong™ Gold Antifade Mountant with DAPI (ThermoFisher #P36935) and stored in the dark for 72 h prior to imaging.

SIM (Structured Illumination Microscopy) images were collected with a Zeiss ELYRA PS.1 super resolution microscope (Carl Zeiss Micro-Imaging) using a 63× oil immersion objective lens with 1.4 NA at room temperature. Three orientation angles of the excitation grid were acquired for each Z plane, with Z spacing of 110 nm between planes. SIM processing was performed with the SIM analysis module of the Zen 2012 BLACK software (Carl Zeiss Micro-Imaging). A three-dimensional reconstruction of SIM data was created using the MARIS software (Bitplane) and exported as tiff images.

Proliferation assay

SaOS2(-/+COPII) cells were plated at 5 × 10^3 cells/well and 143B(-/+COPII) cells were plated at 3 × 10^3 cells/well in a 96-well format. Samples were analyzed in triplicate every 24 h for a total of 96 h for the conversion of 3-(4,5-dimethylthiazol-2-yl)-5-(3-carboxymethoxyphenyl)-2-(4-sulfophenyl)-2H-tetrazolium) (MTS) into soluble formazan (Promega #G5421). After a 1 h incubation the OD was measured on an ELISA plate reader. OD of media alone with these reagents was measured as background and subtracted from test readings.

Invasion assay

SaOS2(-/+COPII) or 143B(-/+COPII) cells were plated at equivalent densities in a collagen-I invasion chamber in the absence of serum (Cell BioLabs#CBA-110-COL). The lower chamber medium contained 10% fetal calf serum, and invasion was analyzed 24 h later by optical density measurements according to the assay protocol.

Proteomic analyses

Two biological replicates of 143B.ST and 143B.ST(+COPII) cells were washed three times with PBS and then replated in serum free medium. After 24 h, culture supernatant was harvested and passed through a 0.22μM filter (Millex-GP SLGP033RS). The filtrate was centrifuged for 5 min at 500 rcf and transferred to new tubes. Cold trichloroacetic acid (100%) was added to samples to a final concentration of 10% TCA. Samples were then briefly vortexed, incubated on ice for 1.5 h, and centrifuged at 15,000 rcf for 10 min at 4Cº. The resulting supernatant was aspirated without disturbing the pellet, which was washed 3× with ice-cold acetone before allowing the pellet to dry for 10 min at room temperature. Pellets were resuspended in 20 μL of 2× Lammeli buffer with 2-β mercaptoethanol and heated to 95°C for 5 min. Solubilized proteins were loaded on a precast 4%–15% gradient gel (BioRad) and run 1 cm into the gel. The gel was then incubated for 1 h in GelCode-Blue (Thermo Scientific), destained overnight in ultrapure H_2O at room temperature, and transferred to our Center for Proteomics and Metabolomics core for proteome profiling by spectral counting.

The stained portion of the gel was cut into small pieces and reduced with dithiothreitol to ensure complete breakage of disulfide bonds. Cysteine residues were alkylated by iodoacetamide to allow the recovery of Cys-containing peptides. The gel segment was washed, dried in a speed vacuum, and rehydrated with a buffer containing trypsin and incubated overnight. The next day the digested samples were acidified, and the peptides were extracted multiple times. The extracts were pooled, dried, and reconstituted in a small volume. The peptide samples were loaded on a nanoscale capillary reverse phase C18 column by a HPLC system (Thermo EasynLC 1000) and eluted by a gradient (~75 min). The eluted peptides were ionized by electrospray ionization and detected by an inline mass spectrometer (Thermo Elite). The MS spectra are collected first, and the 20 most abundant ions were sequentially isolated for MS/MS analysis.

This process was cycled over the entire liquid chromatography gradient. Database searches were performed using Sequest search engine in our in-house SPIDERS software package. All matched MS/MS spectra were filtered by mass accuracy and matching scores to reduce protein false discovery rate to ~1%. Finally, all proteins identified in one gel lane are combined together.

QUANTIFICATION AND STATISTICAL ANALYSIS

RNA expression studies

To analyze real-time PCR results, relative mRNA fold change was computed from the QuantStudio-generated Ct values by using the $2^{-\Delta\Delta Ct}$ method. hFOB1.19 mRNA levels were set to 1, and OS cells mRNA levels were plotted as a relative measure of hFOB1.19 levels. Statistical analyses were performed using Prism Ver. 9 (GraphPad Software) by Student's t-test (unpaired; two-tailed). Error bars indicate mean ± SD. RNA-sequence reads were normalized, and differential analysis performed as relative to hFOB1.19 for the OS cell lines (n = 3) and to normal bone tissue (n = 2) for the OS PDX samples (n = 1). Additionally, RNA expression data derived from OS patient tumor samples are available from the PeCan Database. Data was transformed to log2 and fold change calculated relative to normal bone tissue.

ER area measurement

Transmission electron microscopy images were imported into ImageJ Software and the scale was set based on image calibration. Using the Freehand Selection tool identifiable ER was traced. SaOS2.ST cells were compared to SaOS2.ST(+COPII), n = 4-5 individual cells per cell line with 26–31 total ER regions measured. When 143B.ST cells were compared to 143B.ST(+COL1), n = 3-5 individual cells per cell line with 32 total ER regions measured each cell line. ImageJ area measurements were exported for statistical analyses to Prism Ver. 9 (GraphPad Software) and analyzed by Student's t-test (unpaired; two-tailed). Error bars indicate mean ± SD.

Proliferation assay

Statistical differences of the assay were computed using unpaired, two-tailed Student's t-tests of each timepoint. Differences between SaOS2.ST and SaOS2+COPII, as well as between 143B.ST and 143B + COPII were non-significant. Error bars indicate mean ± SD of 490 nm OD readings, n = 3.

Invasion assay

Statistical differences of the assay between appropriate pairs were computed using unpaired, two-tailed Student's t-tests and Welch's correction. Data are indicated as non-significant (ns). The assay was performed in triplicate. Error bars indicate mean ± SEM of 560 nm OD readings.

Proteomics statistics

In the label-free quantification by spectral-counting (SC) proteomics experiments, the total number of spectra assigned to an individual protein, corresponds to its relative abundance in each sample after normalization for the protein size. For each protein, the summed SC of replicate experiments are compared across samples (e.g., 143bsuntag and 143b64 samples) with missing values replaced by a constant low value to calculate fold change and the p values are derived by using the G-test (Zhou et al., 2010). Proteins changes are considered statistically significant with $p \leq 0.01$ and fold change ≥ 2.